nature structural & molecular biology

ARTICLES

https://doi.org/10.1038/s41594-020-0409-5

Conformational plasticity of the ClpAP AAA+ protease couples protein unfolding and proteolysis

Kyle E. Lopez[1,2,6], Alexandrea N. Rizo[2,3,6], Eric Tse[2], JiaBei Lin[4], Nathaniel W. Scull[5], Aye C. Thwin[2], Aaron L. Lucius[5], James Shorter[4] and Daniel R. Southworth[2]✉

The ClpAP complex is a conserved bacterial protease that unfolds and degrades proteins targeted for destruction. The ClpA double-ring hexamer powers substrate unfolding and translocation into the ClpP proteolytic chamber. Here, we determined high-resolution structures of wild-type *Escherichia coli* ClpAP undergoing active substrate unfolding and proteolysis. A spiral of pore loop–substrate contacts spans both ClpA AAA+ domains. Protomers at the spiral seam undergo nucleotide-specific rearrangements, supporting substrate translocation. IGL loops extend flexibly to bind the planar, heptameric ClpP surface with the empty, symmetry-mismatched IGL pocket maintained at the seam. Three different structures identify a binding-pocket switch by the IGL loop of the lowest positioned protomer, involving release and re-engagement with the clockwise pocket. This switch is coupled to a ClpA rotation and a network of conformational changes across the seam, suggesting that ClpA can rotate around the ClpP apical surface during processive steps of translocation and proteolysis.

The Hsp100 (Clp) AAA+ family of proteins, which are widely present in bacteria and eukaryotes, function as protein unfoldases and disaggregases[1,2]. Conserved members ClpX and ClpA assemble into large proteolytic machines with the serine protease ClpP and serve critical roles in targeted protein degradation and quality control[3–7]. Proteolysis requires substrate recognition and ATP hydrolysis-driven unfolding by the AAA+ domains, which unfold and translocate substrates into the proteolytic chamber of ClpP[8–12]. The ClpP chamber is formed by a double ring of heptamers[13,14], which partner with 1–2 ClpX or ClpA AAA+ hexamers in bacteria, assembling into single- and double-capped complexes[15–17]. To promote client degradation, ClpXP and ClpAP are aided by SspB[18,19] and ClpS[20,21], specificity adaptors that promote recognition of substrates, including those containing the ssrA degron[22,23] and N-end rule substrates[24], respectively. Other substrates, such as the RepA DNA-binding protein, recognized by ClpA, are remodeled or degraded in support of specific cellular functions[3,25].

Hsp100 interactions with ClpP involve a hexamer–heptamer symmetry mismatch, which is a conserved feature among some proteolytic machines, such as the 26S and PAN proteasomes[3,6]. Contacts are mediated by IGF/L motif loops in ClpX or ClpA and hydrophobic binding pockets on the apical surface of ClpP[6,26]. Engagement of these loops triggers an open-gate conformational change of adjacent N-terminal loops on ClpP, facilitating substrate transfer to proteolytic sites[27–29]. Indeed, the acyldepsipeptide class of antibiotics (ADEPs) compete for binding to these pockets and stabilize an open-gate conformation, thereby converting ClpP to an uncontrolled, general protease[30–33]. How these Hsp100–ClpP interactions are coordinated during active unfolding and translocation is unknown.

ClpA contains two nucleotide-binding AAA+ domains (D1 and D2) per protomer, which power unfolding[34]. Structures of related disaggregases, Hsp104 and ClpB, identify the substrate-bound hexamer that adopts a right-handed spiral in which conserved Tyr-bearing pore loops across both AAA+ domains contact and stabilize the polypeptide substrate via backbone interactions spaced every two amino acids[35–38]. Distinct substrate-bound states reveal a ratchet-like mechanism defined by the spiral arrangement, in which the ATP hydrolysis cycle drives substrate release at the lower position and re-binding to the topmost position along the substrate[1,36,39]. A similar spiral architecture and array of substrate contacts has now been identified for many AAA+ machines, supporting a universal rotary translocation mechanism[40–43]. However, for this Hsp100 family it is unclear how the dynamic substrate translocation steps are coupled to proteolysis, or how interactions are maintained at the hexamer–heptamer interface during processive steps of unfolding.

Here, we sought to determine the structural basis for coupled protein unfolding and proteolysis by the ClpAP complex. Using ATP and a RepA-tagged GFP substrate, we determined cryo-EM structures of intact, wild-type ClpAP from *E. coli* to a resolution of ~3.0 Å, which reveal three distinct substrate translocation states. Comparison of these states reveals that the ClpP-connecting IGL loop of the protomer in the lowest substrate-bound position undergoes release and re-binding to the clockwise pocket on ClpP. This IGL-switch movement coincides with a ClpA rotation that is supported by conformational plasticity of five IGL loops, which are bound to the apical surface of ClpP. Nucleotide-specific rearrangements in the AAA+ domains are identified that support a two amino acid-step translocation cycle. Together, these results reveal a model in which IGL loop rearrangements enable ClpA to rotate its position on ClpP consecutively with substrate translocation steps, thereby coupling substrate unfolding with ClpP activity.

Results

Architecture of active, substrate-bound ClpAP. Structures of wild-type ClpAP undergoing active substrate unfolding and proteolysis

[1]Graduate Program in Biophysics, University of California, San Francisco, San Francisco, CA, USA. [2]Department of Biochemistry and Biophysics, Institute for Neurodegenerative Diseases, University of California, San Francisco, San Francisco, CA, USA. [3]Graduate Program in Chemical Biology, University of Michigan, Ann Arbor, MI, USA. [4]Department of Biochemistry and Biophysics, Perelman School of Medicine at the University of Pennsylvania, Philadelphia, PA, USA. [5]Department of Chemistry, The University of Alabama at Birmingham, Birmingham, AL, USA. [6]These authors contributed equally: Kyle E. Lopez, Alexandrea N. Rizo. ✉e-mail: daniel.southworth@ucsf.edu

were desired to capture functional states. RepA-GFP constructs are proteolyzed by ClpAP and can be used to monitor unfolding by ClpA[10,44,45]. Therefore, RepA-GFP containing the first 25 residues of RepA ($RepA^{1-25}$-GFP) was tested for proteolysis and complex formation (Extended Data Fig. 1a–c). While the slowly hydrolysable analog, ATPγS, enables stable formation of AAA+ complexes containing translocated substrates[36,37], the reduced hydrolysis impairs function[10] and may limit the ClpAP conformational cycle. Indeed, substantial degradation of $RepA^{1-25}$-GFP occurs within 15 min in the presence of saturating (10 mM) ATP, while little degradation is observed with ATPγS (Extended Data Fig. 1a). Therefore, to achieve active ClpAP for cryo-EM, incubations were carried out initially with ATPγS to promote assembly and then 10 mM ATP was added to initiate unfolding before vitrification. Assembly with ATPγS and mixtures with ATP have been previously established to support ClpA function[44,46] and we identify that robust degradation occurs under these ATPγS-ATP conditions, indicating that ClpAP is active before vitrification (Extended Data Fig. 1b,c).

In reference-free two-dimensional (2D) class averages, side and top views of ClpP particles double-capped with ClpA predominate (Fig. 1a and Extended Data Fig. 1d). Typically, one ClpA hexamer of the double-capped complex showed well-resolved features, indicating a preferred alignment likely due to flexibility across the double-capped complex. Three-dimensional (3D) classification yielded three distinct ClpAP conformations, which refined to high resolution (2.7–3.2 Å), and hereafter are referred to as Engaged-1 ($ClpAP^{Eng1}$), Disengaged ($ClpAP^{Dis}$) and Engaged-2 ($ClpAP^{Eng2}$) states on the basis of the binding states of the IGL loops (Extended Data Fig. 1e,f). As with 2D analysis, one ClpA hexamer showed improved features over the other. Therefore, the final models included one ClpA hexamer and two ClpP heptamers. In all states the D1 and D2 AAA+ rings of the ClpA hexamer adopt a right-handed spiral, with the D2 ring contacting the planar, heptameric surface of ClpP via the IGL loops (residues 611–623) (Fig. 1b). ClpA is comprised of protomers P1–P6, with P1 at the lowest and P5 at the highest position of the spiral, while P6 is asymmetric and positioned at the seam interface (Fig. 1b). This architecture is similar to related ClpB and Hsp104 double-ring disaggregases in their substrate-bound states[35–37]. Resolution is highest for ClpP (~2.5 Å), while for ClpA it is more variable (~2.5–4.5 Å for $ClpAP^{Eng1}$, ~3–6 Å for $ClpAP^{Dis}$ and ~3–6 Å for $ClpAP^{Eng2}$), with the spiral seam protomers (P1, P5 and P6) at lower resolutions due to their flexibility (Extended Data Fig. 1g–i). The high resolution of the maps permitted accurate atomic models to be built for ClpAP (Fig. 1c, Extended Data Fig. 1j,k and Table 1). Density for the flexible N-terminal (NT) domain of ClpA (residues 1–168) was not well resolved, and thus was not modeled.

Density corresponding to an unfolded polypeptide substrate is identified spanning the D1 and D2 domains in all three structures and modeled as a 24-residue poly-Ala chain (Figs. 1d and 2a–c). Substrate is not observed in the ClpP pore or chamber, which is potentially due to flexibility and the absence of substrate-interacting residues. In low-pass filtered maps of the final reconstruction, globular density at the entrance to the ClpA channel is visible at a reduced threshold that approximately corresponds to a GFP molecule (Extended Data Fig. 1j). These data, together with size-exclusion chromatography (SEC) and proteolysis analysis, indicate that these ClpAP structures, determined under active conditions using ATP, contain RepA-GFP substrate and likely represent conformational states associated with processive translocation and proteolysis.

Structures reveal ClpA IGL loop switches to engage the ClpP symmetry-mismatched pocket. Following multiple rounds of 3D classification, three distinct conformations of substrate-bound ClpAP were refined to high resolution (Fig. 2a–c and Extended Data Fig. 1e,f). The major conformational differences involve ClpA and include changes in substrate interactions and nucleotide states (discussed in the Results below), and changes in the IGL loops and orientation across the ClpA–P interface. No substantial conformational differences are identified for ClpP between the different states (r.m.s. deviation (r.m.s.d.) < 1 Å). In the $ClpAP^{Eng1}$ structure, well-resolved density for the IGL loops from all six ClpA protomers is identified in the pockets around the ClpP apical surface (Fig. 2a,d). One remaining empty pocket on ClpP, which results from the symmetry mismatch of the heptamer, is positioned at the ClpA spiral seam between protomers P1 and P6 (Fig. 2a,d). In the $ClpAP^{Dis}$ structure, density for the IGL loop of protomer P1, which is at the lowest position along the substrate, is no longer observed in the ClpP pocket, resulting in two neighboring empty pockets at the ClpA seam (Fig. 2b,d). Remarkably, in the $ClpAP^{Eng2}$ structure, density for the P1 IGL loop is instead observed in the clockwise adjacent pocket, revealing that the loop has switched position, by comparison with $ClpAP^{Eng1}$, and the empty, symmetry-mismatched pocket

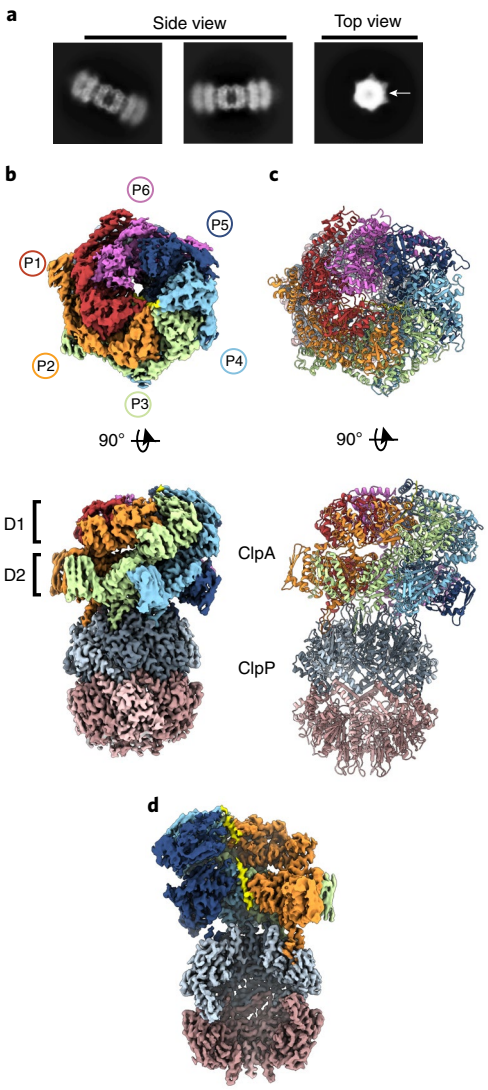

Fig. 1 | Architecture of the substrate-bound ClpAP complex. a, Side and top view 2D class averages of double-capped ClpAP. Rings corresponding to ClpA (arrow) and ClpP rings are identified in the top views. **b**, Top and side views of the final $ClpAP^{Eng1}$ map. **c**, Model of $ClpAP^{Eng1}$. ClpA is colored by individual protomers, as indicated. **d**, Channel view showing substrate peptide bound to ClpA (yellow).

Table 1 | Cryo-EM data collection, refinement and validation statistics of ClpAP^{Eng-1}, ClpAP^{Dis}, ClpAP^{Eng2} and ClpAP—ATPγS

	ClpAP^{Eng1} (EMD-21519, PDB 6W1Z)	ClpAP^{Dis} (EMD-21520, PDB 6W20)	ClpAP^{Eng2} (EMD-21521, PDB 6W21)	Focus ClpAP^{Eng1} (EMD-21522, PDB 6W22)	Focus ClpAP^{Dis} (EMD-21523, PDB 6W23)	Focus ClpAP^{Eng2} (EMD-21524, PDB 6W24)	ClpAP-ATPgS disengaged (EMD-20845, PDB 6UQE)	ClpAP-ATPgS engaged (EMD-20851, PDB 6UQO)
Data collection and processing								
Microscope and camera	Titan Krios, K3	Titan Krios, K3	Titan Krios, K3	Titan Krios, K3	Titan Krios, K3	Titan Krios, K3	Titan Krios, K3	Titan Krios, K3
Magnification	58,600	58,600	58,600	58,600	58,600	58,600	58,600	58,600
Voltage (kV)	300	300	300	300	300	300	300	300
Data acquisition software	Serial EM	Serial EM	Serial EM	Serial EM	Serial EM	Serial EM	Serial EM	Serial EM
Exposure navigation	Image shift	Image shift	Image shift	Image shift	Image shift	Image shift	Image shift	Image shift
Electron exposure ($e^-/Å^2$)	68	68	68	68	68	68	68	68
Defocus range (μm)	0.8–1.2	0.8–1.2	0.8–1.2	0.8–1.2	0.8–1.2	0.8–1.2	1.2–2	1.2–2
Pixel size (Å)	0.853	0.853	0.853	0.853	0.853	0.853	0.853	0.853
Symmetry imposed	*C*1	*C*1	*C*1	*C*1	*C*1	*C*1	*C*1	*C*1
Initial particle images (no.)	739,000	739,000	739,000	739,000	739,000	739,000	1,800,000	1,800,000
Final particle images (no.)	176,232	57,848	39,177	176,232	57,848	39,177	314,000	169,000
Map resolution (Å)	2.7	3.0	3.2	3.0	3.1	3.4	3.0	3.1
FSC threshold	0.143	0.143	0.143	0.143	0.143	0.143	0.143	0.143
Map resolution range (Å)	2–10	2–10	2–10	2.5–10	2.5–10	2.5–10	2–10	2–10
Refinement								
Model resolution (Å)	3.0	3.1	3.2	2.8	3.0	3.3	3.1	3.1
FSC threshold	0.143	0.143	0.143	0.143	0.143	0.143	0.143	0.143
Map sharpening *B* factor ($Å^2$)	−73.0	−68.5	−60.8	−80.3	−65.6	−55.8	−112.9	−103.2
Model composition								
Nonhydrogen atoms	48,556	48,252	48,346	27,542	27,238	27,332	48,402	48,522
Protein residues	6,180	6,134	6,147	3,492	3,446	3,459	6,161	6,174
Ligands	12	12	12	12	12	12	12	12
B factors ($Å^2$)								
Protein	33.4	125.4	177.4	0.5	153.0	210.8	33.7	33.4
Ligand	20.0	151.4	210.6	20.0	151.4	210.6	44.1	20.0
R.m.s. deviations								
Bond lengths (Å)	0.03	0.01	0.011	0.026	0.014	0.013	0.025	0.026
Bond angles (°)	1.76	0.60	0.58	1.81	0.95	0.61	1.82	1.84
Validation								
MolProbity score	1.72	1.96	1.78	1.62	2.26	1.9	1.37	1.25
Clashscore	9.43	13.39	13.92	8.42	15.9	14.4	3.52	2.58
Poor rotamers (%)	0.90	0.20	0.10	0.55	0.03	0.10	0.37	0.08
Ramachandran plot								
Favored (%)	96.58	96.81	96.48	97.07	95.59	97.31	96.55	96.72
Allowed (%)	3.11	3.16	3.20	2.47	4.35	2.51	2.83	2.84
Disallowed (%)	0.31	0.03	0.32	0.46	0.06	0.18	0.62	0.44

now resides between protomers P1 and P2 (Fig. 2c,d). Difference maps of the ClpA–P interface region further validate the position of the P1 IGL loop in these structures (Extended Data Fig. 2). If these structures represented a mix of states then the difference maps would show positive density in both IGL pockets. Importantly, however, positive density for the IGL loop only appears from P1 in the correct ClpP pocket corresponding to the ClpAP^{Eng1} or ClpAP^{Eng2} states, thereby verifying that these structures represent distinct states of the P1 IGL loop. Notably, for ClpAP^{Dis}, density for the P1 IGL loop is not observed in either pocket, indicating that

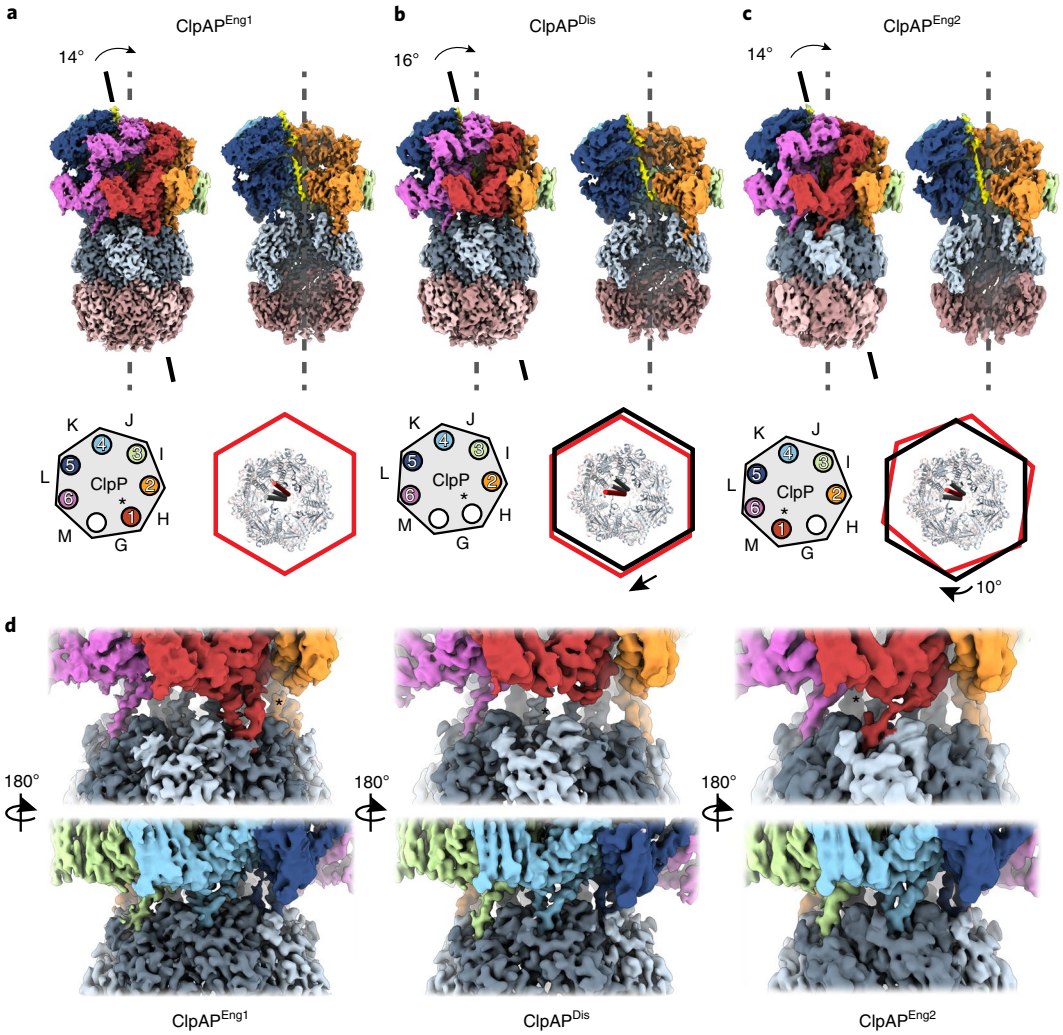

Fig. 2 | Three distinct structures of ClpAP showing IGL loop rearrangement. a–c, Cryo-EM maps for ClpAP^{Eng1} (**a**), ClpAP^{Dis} (**b**) and ClpAP^{Eng2} (**c**) showing the degree offset (arrow) of the ClpA channel axis (solid line) and substrate position (yellow density) compared to the ClpP pore and proteolytic chamber (dashed line). Schematic (lower left) shows occupancy of the ClpA IGL loops (circles, colored and numbered by protomer) around the ClpA hexamer, with the empty IGL pockets (white circles) and ClpA protomers indicated (letters) for the different states. Schematic (lower right) shows top view of ClpP with ClpA as a hexagon overlay (red, current state; black, previous state), and colored cylinders indicating substrate positions (red, current state). **d**, Cryo-EM density of the ClpA–P interface showing IGL loop interaction with ClpP in ClpAP^{Eng1} (left), ClpAP^{Dis} (center) and ClpAP^{Eng2} (right).

this loop is indeed unbound from ClpP and in an intermediate state (Extended Data Fig. 2).

The ClpA channel and bound polypeptide substrate are offset between ~14° and 16° from the ClpP pore in the different structures (Fig. 2a–c). Upon alignment of the structures, ClpA is identified to be in three distinct positions relative to ClpP. These differences appear to occur through a pivot across ClpP and clockwise twist around the substrate channel axis, which coincides with the binding-site switch of the P1 IGL loop (Fig. 2a–c and Supplementary Video 1). Going from the Engaged-1 to the Disengaged state, ClpA pivots towards the P5–P6 side of the hexamer, shifting by approximately 10 Å across ClpP. From the Disengaged to the Engaged-2 states, ClpA twists clockwise, resetting the orientation of the channel relative to ClpA but with an overall rotation of ~10° compared to ClpAP^{Eng1}. The ClpA rotation is visualized in a morph between these states, revealing how protomers P4–P6 tilt towards ClpP, compressing the interface in this region, and then expand through a clockwise rotation around the axial channel in the ClpAP^{Eng2} state (Supplementary Video 1).

In addition to these structures, we determined structures of ATPγS-stabilized ClpAP bound to RepA$^{1-25}$-GFP in which ATP was not added before vitrification (Extended Data Fig. 3). Following similar data classification and refinement procedures, we determined two ClpAP structures at resolutions of 3.0 and 3.1 Å, which match the ClpAP^{Eng1} and ClpAP^{Dis} states described above (Extended Data Fig. 3a–g and Table 1). Notably, the ClpAP^{Eng2} state could not be classified as a distinct conformation despite similar-sized datasets. This could be due to changes in the conformational equilibrium resulting from the ATPγS-stabilized conditions compared to active conditions with ATP. Nonetheless, these structures further establish that the P1 IGL loop undergoes engaged and disengaged conformational changes under conditions in which substrate binding and processing occurs.

IGL loop plasticity enables ClpP engagement by the ClpA spiral. Previous crystal structures of ClpA were unable to resolve the IGL loops due to flexibility, but biochemical data for ClpX IGF loops suggest that they make static interactions with ClpP and that all six IGF loops are required for optimal activity[47]. In the ClpAP structures, density for the ClpA IGL loops is well defined, enabling atomic modeling for nearly all loop residues in each pocket

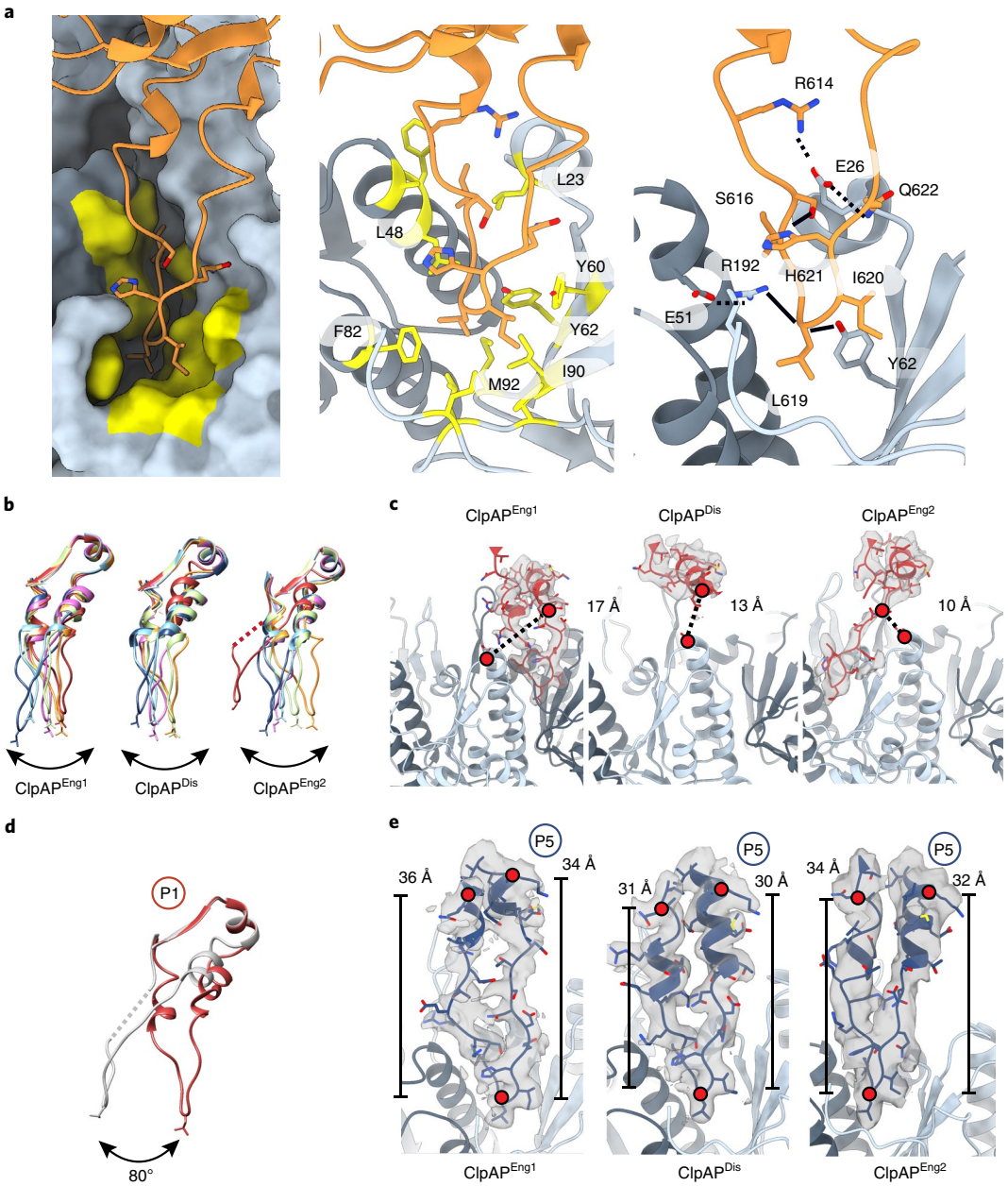

Fig. 3 | IGL loop interactions and conformational flexibility. a, Representative view of a bound IGL loop (orange, ribbon view) positioned in the binding pocket of ClpP, shown in surface view with hydrophobic residues colored in yellow (left), and shown in ribbon views with hydrophobic interactions (middle) and electrostatic contacts (right) labeled. **b**, Overlay of IGL loops (colored by protomer) of $ClpAP^{Eng1}$ (left), $ClpAP^{Dis}$ (middle) and $ClpAP^{Eng2}$ (right). IGL loops are aligned to connecting residues 638–649. Dotted line represents missing residues not present in the density. **c**, Map and model showing that P1 IGL loop density extends into the IGL pocket for $ClpAP^{Eng1}$ (left) and $ClpAP^{Eng2}$ (right) but is disengaged for $ClpAP^{Dis}$ (middle), contacting the adjacent apical ClpP surface (right). The distances between ClpP E67 and ClpA-P1 S625 in the three states are shown to indicate the shift in position of the P1 IGL loop relative to ClpP. **d**, Overlay of IGL loops of P1 for $ClpAP^{Eng1}$ (red) and $ClpAP^{Eng2}$ (gray). **e**, Map and model of the P5 IGL loop for $ClpAP^{Eng1}$ (left), $ClpAP^{Dis}$ (middle) and $ClpAP^{Eng2}$ (right) showing extended and compact conformations, respectively, on the basis of distance measurements between loop residues 605–619 and 633–619 (red dots).

(Extended Data Fig. 4a). The IGL loop region extends from residues N606 and T637, in the base of the D2 large subdomain, as two short α-helices. Residues 616–620 form the flexible loop, which extends into the hydrophobic binding pocket on ClpP, resulting in ~600 $Å^2$ of buried surface area compared to the empty pocket (Fig. 3a, left). The IGL loop binding pocket is formed by the interface of two ClpP protomers and includes α-helices B and C from one protomer and a three-stranded β-sheet (strands 1, 2 and 3) and the C-terminal (CT) strand from the adjacent protomer (Fig. 3a). The loop residues I617, G618, L619 and I620 bind a hydrophobic region in the pocket comprised of A52, L48, F49 and F82 in α-helices of one protomer, and L23, Y60, Y62, I90, M92, F112, L114 and L189 in the adjacent protomer (Fig. 3a, middle). Additional electrostatic contacts likely stabilize the loop as well, including R192 in the CT strand, and E26, which appear to interact with H621 and R614 and Q622, respectively (Fig. 3a, right).

While the IGL loops all make identical contacts with ClpP, flexibility of the connecting helices (residues 608–615 and 624–635)

enables the loops to extend from ClpA in a number of orientations around the hexamer and between the different states (Extended Data Fig. 4b). The largest changes occur with the P1 loop, which switches binding pockets on ClpP between the three states, as discussed above (Fig. 3b–d and Supplementary Video 2). The loop is largely well resolved in the ClpA^{Eng1} and ClpA^{Eng2} states; however, residues 609–624 could not be modeled for ClpA^{Dis} due to weak density in the unbound, disengaged conformation. By comparison of the P1 IGL loop position in the different states, the binding-pocket switch is identified to result from two changes: an overall clockwise rotation of the ClpA hexamer (Fig. 2a–c) and a large 80° rotation of the loop around residues T604 and T637 in the connecting helices (Fig. 3c,d). Surprisingly, the P5 IGL loop is also identified to contract and extend between the states through a partial unfolding of both connecting helices (residues 609–613 and 614–629) (Fig. 3e and Supplementary Video 2). In the Engaged-1 state, the loop is extended by ~5 Å compared to the Disengaged state, whereas in the Engaged-2 state the P5 loop is partially extended by ~3 Å. Notably, this loop extension is only observed at the P5 position and appears to correlate with the orientation of ClpA in the different states. Overall, these results reveal a remarkable conformational plasticity of the IGL loops, which likely functions to support consistent interactions with ClpP around the variable hexamer–heptamer interface during substrate translocation and to enable the binding-pocket switch movement of the P1 loop.

ClpP structure and N-terminal gating. The flexible N-terminal loop residues of ClpP (1–18) form a pore on the apical surface that functions as a substrate gate, which is allosterically controlled by engagement of the adjacent IGF/L-binding pockets by ClpX/A or ADEP compounds[33]. In all three ClpAP structures, the ClpP NT loops from each protomer are well resolved and adopt an extended configuration resulting in an open-gate conformation that is positioned adjacent the ClpA translocation channel, ~30 Å away from where substrate is resolved (Fig. 4a and Extended Data Fig. 5a,b). This is distinct from crystal structures showing that the NT loops adopt an asymmetric open-gate arrangement[48], but similar to ADEP-bound structures where all the loops are in an extended conformation[31,33]. Additionally, no contact is observed between the NT loops and ClpA (Fig. 4a), which may be distinct compared to ClpXP, in which NT loops have been identified to contact the ClpX pore-2 loops[47].

We identify two specific interactions, one across the ClpP NT loops and one with an adjacent helix A in the IGF/L pocket, that have not been previously characterized and appear to stabilize the open-gate conformation (Fig. 4b). A salt-bridge contact between residues R15 in one loop and E14 in the clockwise loop is identified in each protomer (Fig. 4b and Extended Data Fig. 5c). Additionally, a potential salt-bridge contact involving E8 and K25 is also observed, which may additionally stabilize the loop orientation (Fig. 4b and Extended Data Fig. 5d). Notably, K25 is located in a helix that comprises part of the hydrophobic, IGL binding pocket (Fig. 4b). Thus, this interaction may be involved in the allosteric gating mechanism.

For the three structures, both ClpP pores (top and bottom) adopt an open-gate conformation due to the double-capped configuration of the complex. However, in an initial dataset of ATPγS-stabilized ClpAP, we identified a population of single-capped complexes that resolved into one 3D class (Fig. 4c and Extended Data Fig. 5e,f), enabling us to characterize the open- and closed-gate conformations in one structure. While the resolution of the NT loops was not sufficient to model the closed conformation, at lower threshold values, the density for the loops on the unbound end of ClpP appears to extend ~8 Å from ClpP, while density for the ClpA-bound end NT loops extends ~16 Å (Fig. 4d). Additionally, the pore diameter is identified to be ~25 Å for the ClpA-bound end of ClpP, which is substantially wider compared to the unbound end, where the

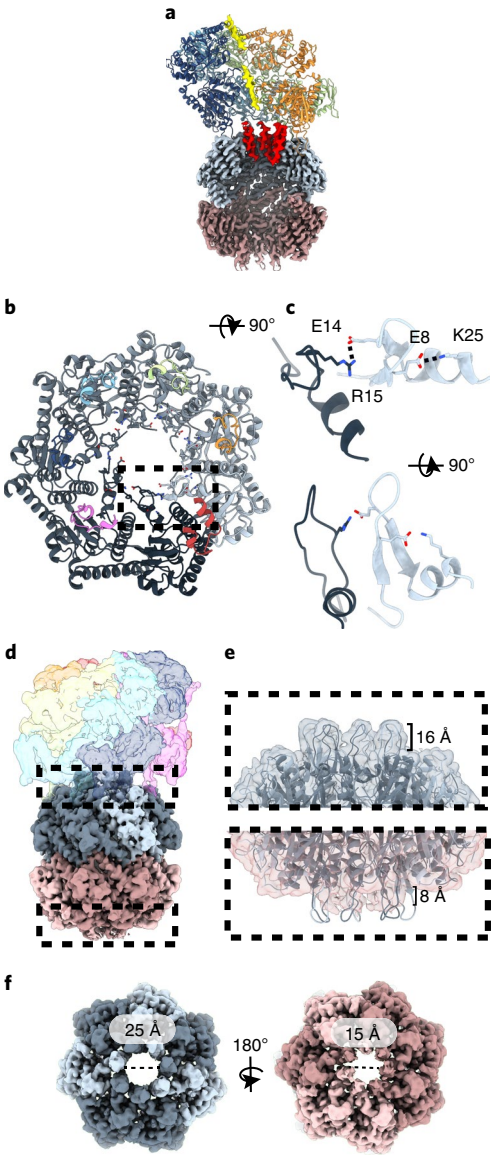

Fig. 4 | Structure of ClpP and NT gating loops. a, Channel view of ClpAP highlighting the ClpP NT gating loops (red) relative to substrate density (yellow). **b**, Top view (left) of ClpP NT loops with ClpA IGL loops (colored by protomer). **c**, Expanded view of an NT loop pair with *cis* (E8–K25) and *trans* (R15–E14) salt-bridge contacts. **d**, Side-view map of single-capped ClpAP complex. **e**, Expanded views of the ClpP pore for the ClpA-bound and unbound surfaces showing open- and closed-gate conformations, respectively. The open-gate conformation was modeled into both sites to show differences compared to the closed-gate density. **f**, Top views showing ClpP pore diameter for the open- (top) and closed- (bottom) gate conformations.

diameter is ~15 Å (Fig. 4e). Thus, we identify that the NT loop gating mechanism is specifically triggered by engagement of the *cis*-bound ClpA IGL loops, which may allosterically regulate the NT loops, potentially through specific salt bridges that stabilize the extended loop arrangement.

ClpA substrate contacts and translocation states. To improve the resolution of the ClpA pore loop interactions and the seam protomers, particle subtraction and focused refinement of the ClpA hexamer were performed (Extended Data Fig. 6a). This resulted in an estimated resolution of 3.0 Å, 3.1 Å and 3.4 Å for the ClpA^{Eng1},

ClpA^{Dis} and ClpA^{Eng2} focused maps, respectively (Extended Data Fig. 6b). While the overall resolution did not increase compared to the full map containing ClpP, improvements in the map density for the seam protomers and substrate contacts was observed, particularly for the Engaged-1 state (Extended Data Fig. 6c–e). Nonetheless, the seam protomers remain at a lower resolution (~3.5–6 Å) compared to the rest of the map, due to their flexibility. Models were further refined using these maps to characterize the substrate interactions and conformational changes between the states. Similar to other AAA+ structures, the conserved Tyr-pore loops in the D1 and D2 domains of ClpA extend into the channel and form a double spiral of substrate interactions spaced every two amino acids along a 24 amino acid-long polypeptide (Fig. 5a). For all states, D1 stabilizes a nine-residue segment through direct contact by Y259 from protomers P1–P4, which intercalates between the substrate side chains and contacts the backbone (Fig. 5b and Extended Data Fig. 6f). The conserved flanking residues, K258 and R260, extend laterally to make electrostatic contacts with the upper and lower adjacent pore loops (D262 and E264), similarly to ClpB D1 (refs. [37,38]). Notably, in the ClpAP^{Eng-1} structure the P5 and P6 D1 pore loops are disconnected from the substrate, with Y259 positioned ~18 Å and ~17 Å away, respectively (Fig. 5a, Extended Data Fig. 6g and Supplementary Video 3). This four-bound, two-unbound configuration of the D1 pore loops is distinct from previous structures of ClpB and Hsp104 (refs. [36–38]). The D2 domain similarly shows well-defined pore loop–substrate contacts for protomers P1–P4 in both states (Fig. 5c and Extended Data Fig. 6f). These interactions stabilize a longer, 11-residue polypeptide segment and are primarily mediated by Y540 and V541, which form a Y-shaped clamp around the substrate backbone. Additional, pore-2 loops[49,50], conserved in ClpB and Hsp104 (refs. [36–38]), are present in both D1 (residues 292–302) and D2 (residues 613–625), and line the channel, likely making additional contributions to stabilizing the polypeptide. Notably, residues E526, R527 and H528 from protomers P1–P5 contact the substrate and together form an 'exit pore' that is adjacent the ClpP gating loops and thus may serve to facilitate transfer to the ClpP chamber (Extended Data Fig. 6h,i).

As with previous Hsp100 structures[36–38], protomers P2–P4 show no substantial conformational changes between the states. Therefore, to compare conformational changes of the seam protomers (P1, P5 and P6), protomer P3 was used for alignments of the ClpA hexamer. The largest changes occur for these protomers between ClpAP^{Eng1} and ClpAP^{Dis}, and between ClpAP^{Eng1} and ClpAP^{Eng2} (r.m.s.d. ≈ 5.1 Å and 3.5 Å, respectively), while changes between ClpAP^{Dis} and ClpAP^{Eng2} are more modest (r.m.s.d. ≈ 2.3 Å). For simplification, comparisons between ClpAP^{Eng1} and ClpAP^{Eng2} are shown (Fig. 5b,c). Overall, the pore loops for P5 and P6 shift closer to the polypeptide substrate and move up the channel axis going from ClpAP^{Eng1} to the ClpAP^{Dis} and ClpAP^{Eng2} states (Fig. 5b,c and Supplementary Video 3). Notably, the P5 pore loop moves up by ~4 Å and towards the substrate by ~8 Å (Extended Data Fig. 6g). This positions P5 Y259 adjacent to the substrate, two residues above the P4 Y259 position supporting the two amino acid translocation step; however, direct contact is not identified. The largest changes occur with the D2 pore loop of protomer P6, which moves up the channel axis by ~7 Å, corresponding to a two-residue shift in the substrate position, but remains unbound to substrate in all three states (Fig. 5c). Together, these changes reveal protomer movements up the channel axis and appear on-path to a translocation step through engagement of the next contact site along the substrate by the D1 in protomer P5 (Extended Data Fig. 6j). To identify how these changes are connected to the IGL loop movement, the Cα deviation between the three states was mapped onto the hexamer model (Fig. 5d). As expected, the IGL loops of the seam protomers show the greatest variability, while protomers P2–P4 show little change. Remarkably, connected regions of variability are identified

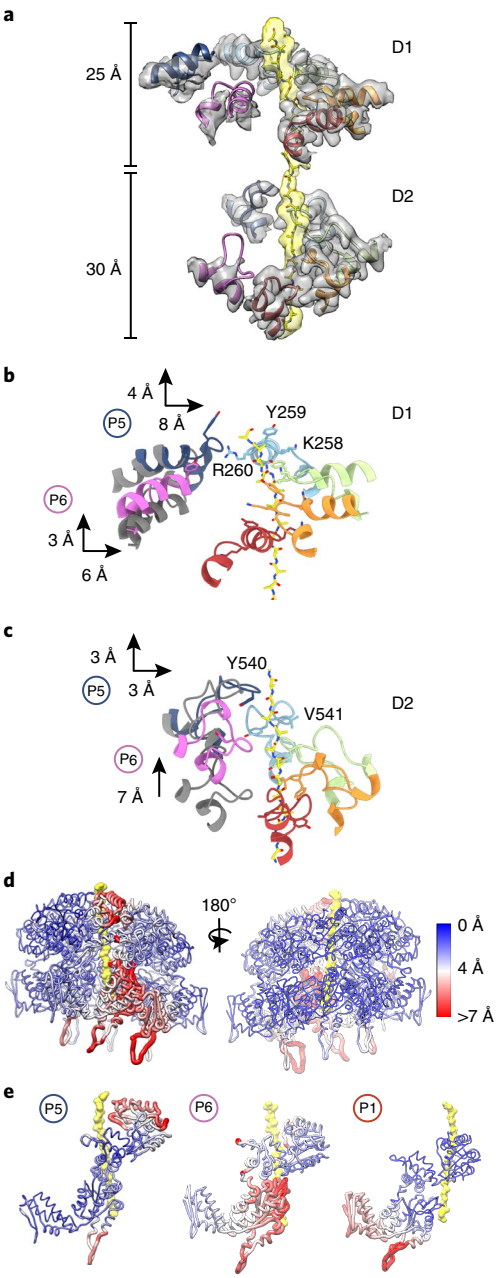

Fig. 5 | ClpA pore loop–substrate contacts and translocation states. **a**, Segmented map and model of the substrate-bound P1–P6 pore loops, colored by protomer, with substrate (yellow) for ClpAP^{Eng1}. Distances shown indicate length of substrate interactions for the D1 and D2. **b**,**c**, Model of the D1 (**b**) and D2 (**c**) pore loops and substrate for ClpAP^{Eng2} (colored by protomer) and overlayed with ClpAP^{Eng1} (gray). Substrate-contacting residues are indicated and shifts in the position of the pore loop protomers, P5 and P6, between states are shown. **d**, ClpAP^{Eng2} model is displayed showing Cα r.m.s.d. between the three states, determined by alignment to protomer P3. Large changes (>7 Å) are indicated in red with wider tubes, intermediate changes (~6.0 Å) are colored in white and small/no changes are colored in blue. **e**, Individual seam protomers shown with Cα r.m.s.d. mapped as in **d** for P5 (left), P6 (middle) and P1 (right).

at the spiral seam across the subdomains and protomer interfaces, revealing a path of conformational changes that extend from the C to the N termini for P1, P6 and P5, respectively. The greatest

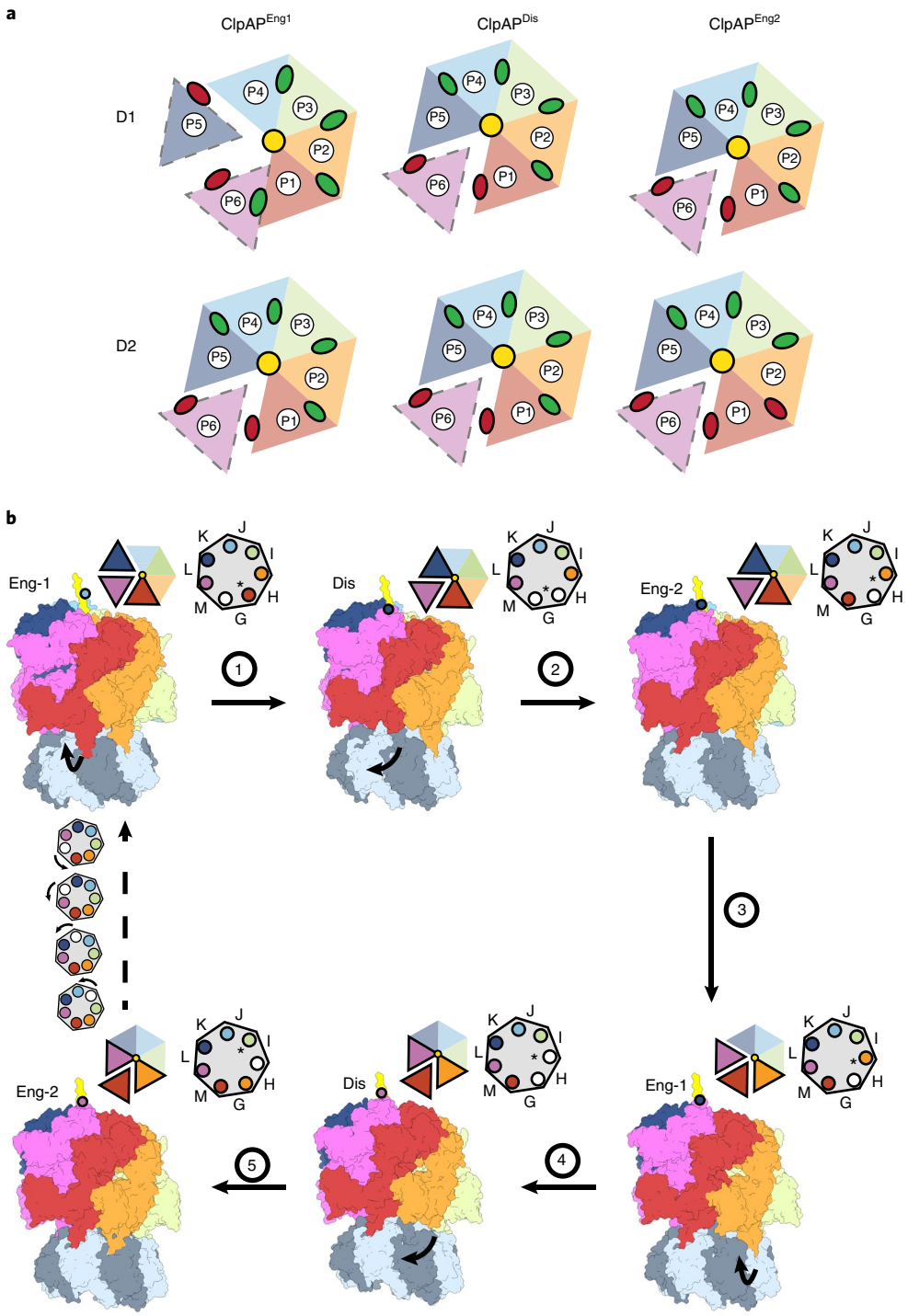

Fig. 6 | Nucleotide states and ClpA rotation model for processive unfolding and proteolysis. a, Schematic showing nucleotide states and substrate contact for D1 and D2 of ClpAP^{Eng1} (left), ClpAP^{Dis} (middle) and ClpAP^{Eng2} (right), determined on the basis of difference maps (Extended Data Fig. 7). Protomer nucleotide states are denoted by colored circles (green for ATP and red for ADP). **b**, Model for ClpAP processive substrate translocation cycle. Two translocation steps are depicted and coupled to IGL loop disengagement (steps 1 and 4) and engagement to the next clockwise IGL pocket on ClpP (steps 2 and 5), indicated by arrows. Top view schematics show the rotary cycle of substrate binding by ClpA (left) and occupancy of ClpP IGL pockets (right). The protomer at the lowest substrate-contact site, which releases the IGL loop, is indicated by an asterisk (*).

variability occurs in the IGL loop and D2 small subdomain of P1, the D2 large subdomain of P6 and the D1 large subdomain of P5 (Fig. 5e and Supplementary Video 4). Remarkably, these changes reveal an 80-Å-long allosteric communication network, which appears to connect IGL loop movement in P1 to translocation steps that occur in P5 and P6.

Nucleotide states support hydrolysis-driven translocation. Similar to Hsp104 and ClpB, ATP hydrolysis activity in D1 and D2 is required for ClpA substrate translocation steps[51]. All three structures show well-resolved nucleotide pockets and the nucleotide state of each pocket was assessed on the basis of the density for ATP and the position of the *trans*-activating Arg-finger residues (R339–R340

in D1 and R643 in D2) (Extended Data Fig. 7). For the substrate-bound protomers P2, P3 and P4, the D1 and D2 nucleotide pockets are largely identical across the three states and in an ATP, active configuration (Fig. 6a and Extended Data Fig. 7a). The D2 of protomer P2 is an exception, and appears to be bound to ADP and in a post-hydrolysis state in ClpAP^{Eng2}. For the seam protomers P1, P5 and P6, the nucleotide states vary, but are similar to previous Hsp100 structures, and thus support models for consecutive hydrolysis during processive translocation previously described[36–38] (Fig. 6a and Extended Data Fig. 7b). The P5 D1 appears to switch from an ADP state in ClpA^{Eng1} to an ATP state in ClpA^{Dis} and ClpA^{Eng2}, indicating that nucleotide exchange may occur between these states. Notably, this coincides with the conformational changes that bring the P5 D1 pore loop towards the next contact position along the substrate after P4 (Fig. 5b), supporting models proposing that the translocation step occurs upon ATP re-binding[1]. Conversely, the P5 D2 domain is in an ATP state and bound to substrate in all three structures (Fig. 6a and Extended Data Fig. 7b). Protomer P6, which is at the spiral seam and unbound to substrate, is in a post-hydrolysis, ADP state for both D1 and D2 across all three structures. For protomer P1, which is at the lowest substrate-contact position and undergoes IGL loop switching between the states, the D1 appears bound to ATP in ClpA^{Eng1} and bound to ADP in ClpA^{Dis} and ClpA^{Eng2}, indicating that hydrolysis likely occurs between these states. However, the P1 D2 appears bound to ADP and inactive in all states, based on the distal position of the Arg finger.

Together, the changes in nucleotide states between the three structures indicate that ATP hydrolysis occurs at the spiral seam and likely proceeds counterclockwise around the hexamer, supporting the rotary substrate translocation cycle in which protomers towards low position in the spiral (P1 and P2) undergo ATP hydrolysis and substrate release, then re-bind substrate at the top position (P5) with ATP binding[1] (Fig. 6a and Extended Data Fig. 7a). On the basis of the different D1 and D2 nucleotide states within protomers P1, P2 and P5, hydrolysis may be asynchronous, and possibly initiated in the D2 ring based on the ATP–ADP change identified for P2 between the ClpA^{Dis} and ClpA^{Eng2} structures. This finding is reminiscent of observations made with ClpB[37]. Moreover, it indicates that in ClpA, D1 and D2 regulate distinct steps of translocation and coordination with ClpP. Surprisingly, certain conformational changes, including release of substrate, movement of the P1 IGL loop and changes in P6, do not appear to directly correlate with changes in the *cis* nucleotide pocket. Allosteric communication and distinct functional roles have been described for the D1 and D2 of ClpB[52,53]. Thus, hydrolysis at adjacent sites, either across D1 and D2 or between protomers connected by the Arg finger, may allosterically drive the conformational changes identified in the different structures. Indeed, the P1 IGL loop switching may be supported by hydrolysis at P1 D1 during disengagement (ClpA^{Eng1} to ClpA^{Dis}) and at P2 D2 during engagement of the next pocket (ClpA^{Dis} to ClpA^{Eng2}) (Fig. 6a and Extended Data Fig. 7b).

Discussion

For the conserved class of AAA+ protease complexes, such as ClpXP and ClpAP, it has been unclear how dynamic steps of ATP hydrolysis-driven substrate translocation could occur in coordination with the attached heptameric protease. The structures presented here reveal a dynamic ClpA–P interface, in which the connecting IGL loops undergo large conformational changes that may enable the ClpA hexamer to rotate on the ClpP apical surface during processive translocation steps (Fig. 2). Most notably, the IGL loop of the protomer in the lowest substrate-bound site (P1) is observed in three different positions, which, together, reveal a clockwise binding-pocket switch movement. This IGL loop movement appears to be coordinated with conformational changes associated with the substrate translocation steps, based on the large allosteric communication path we identify across the seam protomers, which connects ClpP interactions with the pore loop–substrate contacts (Fig. 5d).

The conformational differences between the three structures suggest a model for substrate translocation by ClpAP in which hexamer–heptamer symmetry mismatch is continually maintained with an empty IGL binding pocket aligned at the spiral seam of ClpA. During consecutive translocation steps, the IGL loop of the adjacent protomer (P1) at the lowest substrate-contact site disengages from ClpP (ClpAP^{Eng1} to ClpAP^{Dis}, step 1) then re-binds to the clockwise empty pocket (ClpAP^{Dis} to ClpAP^{Eng2}, step 2) in a manner that is regulated by ATP hydrolysis and conformational changes associated with substrate release and re-binding (Fig. 6b and Supplementary Video 5). On the basis of the path of conformational variability (Fig. 5d) and changes in nucleotide state (Fig. 6a) across the seam protomers, ATP hydrolysis and translocation movements by neighboring protomers likely regulate the P1 IGL loop movement, coordinating the binding-pocket switch with translocation steps.

The nucleotide states of the protomers and pore loop spacing along the substrate are consistent with a rotary, two amino acid-step translocation mechanism proposed in previous studies[35–37,43]. This step size is smaller than has been reported for ClpA and ClpX by single-molecule[54,55] and transient-state kinetic methods[56]. However, recent single-molecule studies of ClpB identify rapid modes of consecutive translocation in which 6–7-Å steps could occur but are not resolvable due to the high translocation rate[57]. For a processive cycle[2,58,59], we propose that these steps could continue with IGL loop switching at each translocation step, rotating the position of the empty IGL pocket around ClpP with the spiral seam (Fig. 6b). This rotation of ClpA relative to ClpP would enable the hexamer to shift by one clockwise binding position on the ClpP apical surface per six substrate translocation steps down the axial channel. Other models involving larger translocation step sizes[55] or alternative hydrolysis mechanisms[60] would likely confer different coordination with IGL loop switching. Nonetheless, we suggest that the functional importance of the hexamer–heptamer mismatch is that the seventh binding pocket on ClpP is available for the IGL loops to sequentially switch position with the substrate translocation steps, allowing processivity by ClpA without altering contact with ClpP. Additionally, this rotation may be substrate specific and perhaps more critical for the proteolysis of stable, folded substrates compared to labile structures.

While other mechanisms may support substrate translocation and proteolysis by ClpAP, we note that IGL loop switching between the same sites, stochastically or counterclockwise, would result in an offset between the empty IGL pocket and the spiral seam of the ClpA hexamer. None of these potential configurations of ClpAP were observed in any of the 3D classes for our ATPγS and ATP datasets. Additionally, recent structures of the related ClpXP complex bound to substrate identify conformations that are similar to the Engaged-1 and Disengaged states determined here, and a complementary rotary mechanism is proposed[61]. The additional Engaged-2 state structure determined here further supports these models by identifying that the P1 IGL loop indeed switches position, and ClpA rotates clockwise relative to ClpP with an apparent substrate translocation step. The discovery of this additional state in our study may have resulted from the use of wild-type enzyme and ATP, allowing an additional active state of substrate translocation to be captured.

The IGL loop interactions with the ClpP hydrophobic pockets are identical at all positions, while flexibility of the helices that connect the loops to the D2 base of ClpA enables substantial variability in the ClpA position relative to ClpP. This flexibility is likely critical for maintaining ClpP binding during ratcheting conformational changes associated with substrate translocation and the rotations in ClpA between the different states (Fig. 2a–c). Furthermore, the extension and unfolding of the P5 IGL loop helices in the Engaged-1

state is striking and may also provide energetic constraints that could facilitate release and clockwise switch of the P1 IGL loop during the conformational change to the Disengaged and Engaged-2 states (Fig. 3c).

Binding by IGF/L loops is well understood to trigger gate opening in ClpP[27–29], and the conformational plasticity and asymmetric binding interactions we identify reveal new insight into how these loops facilitate allosteric regulation between ClpA and ClpP[56,62]. A number of proteolytic machines, including the 26S proteasome, operate as hexamer–heptamer assemblies[3,4]. Notably, assembly of the eukaryotic Rpt and archaeal PAN AAA+ with its respective 20S core involve interaction with flexible C-terminal HbYX motifs and gate opening of the 20S core[63,64]. While the HbYX interactions are distinct and likely operate differently during translocation, recent structures reveal a conserved spiral staircase arrangement of 26S[41,65] and PAN[66] bound to substrates, and a sequential rotation of the ATPase ring has been proposed for PAN[66]. For the Clp protease system the symmetry mismatch and IGF/L loop binding-pocket switch likely serves a critical role in processivity by coordinating the rotary ATPase cycle and directional translocation steps with substrate transfer and proteolysis by ClpP.

Online content

Any methods, additional references, Nature Research reporting summaries, source data, extended data, supplementary information, acknowledgements, peer review information; details of author contributions and competing interests; and statements of data and code availability are available at https://doi.org/10.1038/s41594-020-0409-5.

Received: 22 October 2019; Accepted: 9 March 2020;
Published online: 20 April 2020

References

1. Shorter, J. & Southworth, D. R. Spiraling in control: structures and mechanisms of the Hsp104 disaggregase. *Cold Spring Harb. Perspect. Biol.* **11**, a034033 (2019).
2. Duran, E. C., Weaver, C. L. & Lucius, A. L. Comparative analysis of the structure and function of AAA+ motors ClpA, ClpB, and Hsp104: common threads and disparate functions. *Front. Mol. Biosci.* **4**, 54 (2017).
3. Olivares, A. O., Baker, T. A. & Sauer, R. T. Mechanistic insights into bacterial AAA+ proteases and protein-remodelling machines. *Nat. Rev. Microbiol.* **14**, 33–44 (2016).
4. Sauer, R. T. & Baker, T. A. AAA+ proteases: ATP-fueled machines of protein destruction. *Annu. Rev. Biochem.* **80**, 587–612 (2011).
5. Sauer, R. T. et al. Sculpting the proteome with AAA$^+$ proteases and disassembly machines. *Cell* **119**, 9–18 (2004).
6. Kessel, M. et al. Homology in structural organization between *E. coli* ClpAP protease and the eukaryotic 26S proteasome. *J. Mol. Biol.* **250**, 587–594 (1995).
7. Sousa, M. C. et al. Crystal and solution structures of an HslUV protease–chaperone complex. *Cell* **103**, 633–643 (2000).
8. Baker, T. A. & Sauer, R. T. ClpXP, an ATP-powered unfolding and protein-degradation machine. *Biochim. Biophys. Acta* **1823**, 15–28 (2012).
9. Reid, B. G., Fenton, W. A., Horwich, A. L. & Weber-Ban, E. U. ClpA mediates directional translocation of substrate proteins into the ClpP protease. *Proc. Natl Acad. Sci. USA* **98**, 3768–3772 (2001).
10. Hoskins, J. R., Pak, M., Maurizi, M. R. & Wickner, S. The role of the ClpA chaperone in proteolysis by ClpAP. *Proc. Natl Acad. Sci. USA* **95**, 12135–12140 (1998).
11. Weber-Ban, E. U., Reid, B. G., Miranker, A. D. & Horwich, A. L. Global unfolding of a substrate protein by the Hsp100 chaperone ClpA. *Nature* **401**, 90–93 (1999).
12. Ishikawa, T. et al. Translocation pathway of protein substrates in ClpAP protease. *Proc. Natl Acad. Sci. USA* **98**, 4328–4333 (2001).
13. Wang, J., Hartling, J. A. & Flanagan, J. M. The structure of ClpP at 2.3 Å resolution suggests a model for ATP-dependent proteolysis. *Cell* **91**, 447–456 (1997).
14. Yu, A. Y. & Houry, W. A. ClpP: a distinctive family of cylindrical energy-dependent serine proteases. *FEBS Lett.* **581**, 3749–3757 (2007).
15. Grimaud, R., Kessel, M., Beuron, F., Steven, A. C. & Maurizi, M. R. Enzymatic and structural similarities between the *Escherichia coli* ATP-dependent proteases, ClpXP and ClpAP. *J. Biol. Chem.* **273**, 12476–12481 (1998).
16. Ortega, J., Lee, H. S., Maurizi, M. R. & Steven, A. C. ClpA and ClpX ATPases bind simultaneously to opposite ends of ClpP peptidase to form active hybrid complexes. *J. Struct. Biol.* **146**, 217–226 (2004).
17. Ortega, J., Singh, S. K., Ishikawa, T., Maurizi, M. R. & Steven, A. C. Visualization of substrate binding and translocation by the ATP-dependent protease, ClpXP. *Mol. Cell* **6**, 1515–1521 (2000).
18. Levchenko, I., Seidel, M., Sauer, R. T. & Baker, T. A. A specificity-enhancing factor for the ClpXP degradation machine. *Science* **289**, 2354–2356 (2000).
19. Bolon, D. N., Grant, R. A., Baker, T. A. & Sauer, R. T. Nucleotide-dependent substrate handoff from the SspB adaptor to the AAA+ ClpXP protease. *Mol. Cell* **16**, 343–350 (2004).
20. Erbse, A. et al. ClpS is an essential component of the N-end rule pathway in *Escherichia coli*. *Nature* **439**, 753–756 (2006).
21. Wang, K. H., Roman-Hernandez, G., Grant, R. A., Sauer, R. T. & Baker, T. A. The molecular basis of N-end rule recognition. *Mol. Cell* **32**, 406–414 (2008).
22. Keiler, K. C., Waller, P. R. & Sauer, R. T. Role of a peptide tagging system in degradation of proteins synthesized from damaged messenger RNA. *Science* **271**, 990–993 (1996).
23. Gottesman, S., Roche, E., Zhou, Y. & Sauer, R. T. The ClpXP and ClpAP proteases degrade proteins with carboxy-terminal peptide tails added by the SsrA-tagging system. *Genes Dev.* **12**, 1338–1347 (1998).
24. Mogk, A., Schmidt, R. & Bukau, B. The N-end rule pathway for regulated proteolysis: prokaryotic and eukaryotic strategies. *Trends Cell Biol.* **17**, 165–172 (2007).
25. Wickner, S. et al. A molecular chaperone, ClpA, functions like DnaK and Dna. *Proc. Natl Acad. Sci. USA* **91**, 12218–12222 (1994).
26. Kim, Y. I. et al. Molecular determinants of complex formation between Clp/Hsp100 ATPases and the ClpP peptidase. *Nat. Struct. Biol.* **8**, 230–233 (2001).
27. Effantin, G., Maurizi, M. R. & Steven, A. C. Binding of the ClpA unfoldase opens the axial gate of ClpP peptidase. *J. Biol. Chem.* **285**, 14834–14840 (2010).
28. Bewley, M. C., Graziano, V., Griffin, K. & Flanagan, J. M. Turned on for degradation: ATPase-independent degradation by ClpP. *J. Struct. Biol.* **165**, 118–125 (2009).
29. Jennings, L. D., Bohon, J., Chance, M. R. & Licht, S. The ClpP N-terminus coordinates substrate access with protease active site reactivity. *Biochemistry* **47**, 11031–11040 (2008).
30. Brotz-Oesterhelt, H. et al. Dysregulation of bacterial proteolytic machinery by a new class of antibiotics. *Nat. Med.* **11**, 1082–1087 (2005).
31. Lee, B. G. et al. Structures of ClpP in complex with acyldepsipeptide antibiotics reveal its activation mechanism. *Nat. Struct. Mol. Biol.* **17**, 471–478 (2010).
32. Gersch, M. et al. AAA+ chaperones and acyldepsipeptides activate the ClpP protease via conformational control. *Nat. Commun.* **6**, 6320 (2015).
33. Li, D. H. et al. Acyldepsipeptide antibiotics induce the formation of a structured axial channel in ClpP: a model for the ClpX/ClpA-bound state of ClpP. *Chem. Biol.* **17**, 959–969 (2010).
34. Wendler, P., Ciniawsky, S., Kock, M. & Kube, S. Structure and function of the AAA+ nucleotide binding pocket. *Biochim. Biophys. Acta* **1823**, 2–14 (2012).
35. Deville, C. et al. Structural pathway of regulated substrate transfer and threading through an Hsp100 disaggregase. *Sci. Adv.* **3**, e1701726 (2017).
36. Gates, S. N. et al. Ratchet-like polypeptide translocation mechanism of the AAA+ disaggregase Hsp104. *Science* **357**, 273–279 (2017).
37. Rizo, A. N. et al. Structural basis for substrate gripping and translocation by the ClpB AAA+ disaggregase. *Nat. Commun.* **10**, 2393 (2019).
38. Yu, H. et al. ATP hydrolysis-coupled peptide translocation mechanism of *Mycobacterium tuberculosis* ClpB. *Proc. Natl Acad. Sci. USA* **115**, E9560–E9569 (2018).
39. Gates, S. N. & Martin, A. Stairway to translocation: AAA+ motor structures reveal the mechanisms of ATP-dependent substrate translocation. *Protein Sci.* **29**, 407–419 (2020).
40. Han, H., Monroe, N., Sundquist, W. I., Shen, P. S. & Hill, C. P. The AAA ATPase Vps4 binds ESCRT-III substrates through a repeating array of dipeptide-binding pockets. *Elife* **6**, e31324 (2017).
41. de la Pena, A. H., Goodall, E. A., Gates, S. N., Lander, G. C. & Martin, A. Substrate-engaged 26S proteasome structures reveal mechanisms for ATP-hydrolysis-driven translocation. *Science* **362**, e31324 (2018).
42. Ho, C. M. et al. Malaria parasite translocon structure and mechanism of effector export. *Nature* **561**, 70–75 (2018).
43. Puchades, C. et al. Structure of the mitochondrial inner membrane AAA+ protease YME1 gives insight into substrate processing. *Science* **358**, eaao0464 (2017).
44. Hoskins, J. R., Singh, S. K., Maurizi, M. R. & Wickner, S. Protein binding and unfolding by the chaperone ClpA and degradation by the protease ClpAP. *Proc. Natl Acad. Sci. USA* **97**, 8892–8897 (2000).
45. Hoskins, J. R. & Wickner, S. Two peptide sequences can function cooperatively to facilitate binding and unfolding by ClpA and degradation by ClpAP. *Proc. Natl Acad. Sci. USA* **103**, 909–914 (2006).
46. Miller, J. M. & Lucius, A. L. ATPγS competes with ATP for binding at Domain 1 but not Domain 2 during ClpA catalyzed polypeptide translocation. *Biophys. Chem.* **185**, 58–69 (2014).

47. Martin, A., Baker, T. A. & Sauer, R. T. Distinct static and dynamic interactions control ATPase–peptidase communication in a AAA+ protease. *Mol. Cell* **27**, 41–52 (2007).
48. Bewley, M. C., Graziano, V., Griffin, K. & Flanagan, J. M. The asymmetry in the mature amino-terminus of ClpP facilitates a local symmetry match in ClpAP and ClpXP complexes. *J. Struct. Biol.* **153**, 113–128 (2006).
49. Hinnerwisch, J., Fenton, W. A., Furtak, K. J., Farr, G. W. & Horwich, A. L. Loops in the central channel of ClpA chaperone mediate protein binding, unfolding, and translocation. *Cell* **121**, 1029–1041 (2005).
50. Martin, A., Baker, T. A. & Sauer, R. T. Diverse pore loops of the AAA+ ClpX machine mediate unassisted and adaptor-dependent recognition of ssrA-tagged substrates. *Mol. Cell* **29**, 441–450 (2008).
51. Kress, W., Mutschler, H. & Weber-Ban, E. Both ATPase domains of ClpA are critical for processing of stable protein structures. *J. Biol. Chem.* **284**, 31441–31452 (2009).
52. Mogk, A. et al. Roles of individual domains and conserved motifs of the AAA+ chaperone ClpB in oligomerization, ATP hydrolysis, and chaperone activity. *J. Biol. Chem.* **278**, 17615–17624 (2003).
53. Fernandez-Higuero, J. A. et al. Allosteric communication between the nucleotide binding domains of caseinolytic peptidase B. *J. Biol. Chem.* **286**, 25547–25555 (2011).
54. Olivares, A. O., Nager, A. R., Iosefson, O., Sauer, R. T. & Baker, T. A. Mechanochemical basis of protein degradation by a double-ring AAA+ machine. *Nat. Struct. Mol. Biol.* **21**, 871–875 (2014).
55. Aubin-Tam, M. E., Olivares, A. O., Sauer, R. T., Baker, T. A. & Lang, M. J. Single-molecule protein unfolding and translocation by an ATP-fueled proteolytic machine. *Cell* **145**, 257–267 (2011).
56. Miller, J. M., Lin, J., Li, T. & Lucius, A. L. *E. coli* ClpA catalyzed polypeptide translocation is allosterically controlled by the protease ClpP. *J. Mol. Biol.* **425**, 2795–2812 (2013).
57. Avellaneda, M. J. et al. Processive extrusion of polypeptide loops by a Hsp100 disaggregase. *Nature* **578**, 317–320 (2020).
58. Lee, C., Schwartz, M. P., Prakash, S., Iwakura, M. & Matouschek, A. ATP-dependent proteases degrade their substrates by processively unraveling them from the degradation signal. *Mol. Cell* **7**, 627–637 (2001).
59. Olivares, A. O., Kotamarthi, H. C., Stein, B. J., Sauer, R. T. & Baker, T. A. Effect of directional pulling on mechanical protein degradation by ATP-dependent proteolytic machines. *Proc. Natl Acad. Sci. USA* **114**, E6306–E6313 (2017).
60. Cordova, J. C. et al. Stochastic but highly coordinated protein unfolding and translocation by the ClpXP proteolytic machine. *Cell* **158**, 647–658 (2014).
61. Ripstein, Z. A., Vahidi, S., Houry, W. A., Rubinstein, J. L. & Kay, L. E. A processive rotary mechanism couples substrate unfolding and proteolysis in the ClpXP degradation machinery. *Elife* **9**, e52158 (2020).
62. Rajendar, B. & Lucius, A. L. Molecular mechanism of polypeptide translocation catalyzed by the *Escherichia coli* ClpA protein translocase. *J. Mol. Biol.* **399**, 665–679 (2010).
63. Rabl, J. et al. Mechanism of gate opening in the 20S proteasome by the proteasomal ATPases. *Mol. Cell* **30**, 360–368 (2008).
64. Smith, D. M. et al. Docking of the proteasomal ATPases' carboxyl termini in the 20S proteasome's α ring opens the gate for substrate entry. *Mol. Cell* **27**, 731–744 (2007).
65. Dong, Y. et al. Cryo-EM structures and dynamics of substrate-engaged human 26S proteasome. *Nature* **565**, 49–55 (2019).
66. Majumder, P. et al. Cryo-EM structures of the archaeal PAN-proteasome reveal an around-the-ring ATPase cycle. *Proc. Natl Acad. Sci. USA* **116**, 534–539 (2019).

Methods

Purification and analysis of ClpA, ClpP and RepA$^{1-25}$-GFP. ClpA and ClpP were purified as previously described[56,67]. RepA$^{1-25}$ protein was expressed with a C-terminal His6-tag construct from the pDS56/RBSII plasmid. Transformed BL21 cells were inoculated in LB media with 100 μg ml^{-1} ampicillin and grown at 37 °C to optical density at 600 nm, OD_{600} = ~0.6–0.8. The cell culture was induced with 1 mM IPTG for ~4 h at 30 °C. The cell pellet was resuspended in 40 mM HEPES pH 7.4, 2 mM β-mercaptoethanol and 10% glycerol with protease inhibitors (EDTA-free) (Roche) and then lysed by sonication. Following centrifugation (16,000*g*, 20 min, 30 °C), the supernatant was applied to a Ni-NTA column (GE Healthcare) followed by a gradient elution from 20 mM imidazole to 500 mM imidazole. Purity was verified by SDS–PAGE and fractions were combined and concentrated into a storage buffer (40 mM HEPES pH 7.4, 500 mM KCl, 20 mM $MgCl_2$, 10% glycerol (v/v) and 2 mM β-mercaptoethanol).

The RepA$^{1-25}$-GFP degradation assay (Extended Data Fig. 1a,b) was performed in triplicate and consisted of 6 μM ClpA, 7 μM ClpP or ClpP-S98A, 1 μM RepA$^{1-25}$-GFP and 2 mM nucleotide incubated in buffer at 20°C for 15 min containing 50 mM Tris–HCl pH 7.5, 150 mM KCl, 10 mM $MgCl_2$ and 1 mM DTT. For the assay with spiked nucleotide, 10 mM nucleotide was added after the initial incubation. Aliquots of the reaction were separated from the reaction at the specified time points and quenched in 2% SDS buffer, heated for 10 min and run onto an acrylamide gel. The bands were visualized using silver staining (SigmaAldrich). SEC analysis and purification were performed by incubating 36 μM ClpA, 42 μM ClpP, 30 μM RepA$^{1-25}$-GFP and 2 mM ATPγS in 50 mM Tris–HCl pH 7.5, 150 mM KCl, 10 mM $MgCl_2$, 1 mM DTT for 15 min at 20°C. The complex incubation reaction was then injected onto a Superose 6 Increase 3.2/300 column (GE Healthcare) and the eluted peaks were analyzed using SDS–PAGE.

Cryo-EM data collection and processing. The fraction corresponding to the largest molecular weight complex from SEC (Extended Data Fig. 1b) was isolated and incubated with 1 mM ATPγS. Before freezing, proper dilutions were made and 10 mM ATP was added to the dilution. After a 30-s incubation, a 3.5-μl drop was applied to a glow-discharged holey carbon grid (R 1.2/1.3; Quantifoil), in which the sample was then blotted for 2.5 s at 4°C and 100% humidity with Whatman no. 595 filter paper before being plunge frozen in liquid ethane using a vitrobot (ThermoFisher Scientific). The sample was then imaged on a Titan Krios TEM (ThermoFisher Scientific) operated at 300 keV and equipped with a Gatan BioQuantum imaging energy filter using a 20-eV zero loss energy slit (Gatan). Movies were acquired in super-resolution mode on a K3 direct electron detector (Gatan) at a calibrated magnification of ×58,600 corresponding to a pixel size of 0.4265 Å per pixel. A defocus range of 0.8 to 1.2 μm was used with a total exposure time of 2 s fractionated into 0.2-s subframes for a total dose of 68 $e^-/Å^2$ at a dose rate of 25 e^- per pixel per second. Movies were subsequently corrected for drift using MotionCor2 (ref. [68]) and were Fourier cropped by a factor of 2 to a final pixel size of 0.853 Å per pixel.

A total of ~18,000 micrographs were collected over two different datasets. The two datasets were processed separately and then combined at the end. All the data processing was performed in cryosparc2 (ref. [69]). For particle picking, templates were generated from 100 particles, in which only side views were selected. After inspecting the particles picked, approximately 1.6 million particles were extracted. Two rounds of 2D classification were performed to remove contamination and junk particles, which amounted to ~54% of the dataset. A five-class ab-initio reconstruction was performed from the particle set and was used for initial classification steps.

To identify different conformations, heterogeneous refinement was performed with four different classes (Extended Data Fig. 1f). Following this first round, maps showing high-resolution features, which accounted for ~54% of the 739,000 particles going into 3D, were kept and grouped together. Another round of heterogeneous refinement with five different classes was then performed. Following this second round, two unique states, ClpAP^{Eng1} (24%, ~176,000 particles) and ClpAP^{Dis} (24%, ~176,000 particles), were identified. The ClpAP^{Dis} particles underwent another five-class heterogeneous refinement to further identify any more conformations. Following this third round, two unique states, ClpAP^{Dis} (8%, 58,000 particles) and ClpAP^{Eng2} (5%, 40,000 particles), were identified. Particles associated with each unique class were combined and homogeneous refinement was performed separately on each state. To better improve the resolution of the mobile protomers following nonuniform refinement, the particles from each state underwent particle subtraction. Particle subtraction was performed in which the bottom half of ClpP was subtracted. A local refinement was then performed, in which the fulcrum position was set to the center of ClpA. The same procedure was completed on all the states.

The final resolution for ClpAP^{Eng1} was 2.8 Å, for ClpAP^{Dis} was 3.2 Å and for ClpAP^{Eng2} was 3.4 Å (Extended Data Fig. 6b). After completing local CTF refinement on the final refinement runs, the resolutions were improved to 2.7 Å for ClpAP^{Eng1}, 3.0 Å for ClpAP^{Dis} and 3.2 Å for ClpAP^{Eng2} (Extended Data Fig. 1e).

Molecular modeling. An initial model for ClpA was obtain by using a ClpB structure (PDB 5OFO)[35] and generated in SWISS-MODEL[70] and the initial model for ClpP was taken directly from a ClpP crystal structure (PDB 1YG6)[48] previously solved. Both initial models were docked into the EM maps using UCSF Chimera's function fit in map[71]. Initial refinement was performed using Phenix[72] with one round of simulated annealing and morphing and five rounds of real-space refinement that included minimization_global, rigid_body, adp, local_grid_search, secondary structural restraints and noncrystallographic symmetry restraints. The resulting model then underwent real-space refinement in Coot[73]. Nucleotides were added in manually using Coot and real-space refinement using cif files generated for ADP and ATPγS in Phenix eLBOW[74].

Density for the ClpA focus refinement was higher quality than for the full map, and so was used to model individual protomers using Rosetta comparitive modeling (RosettaCM)[75,76]. The structures for ClpA (PDB 1R6B)[77], Hsp104 (PDB 5D4W and 5VJH)[36], ClpB BAP form (PDB 5OG1)[35] and PTEX (PDB 6E10)[42] were determined as homology models with HHpred[78] and used to constrain model refinement in RosettaCM with template_weight = 0 and the initial model with template_weight = 1. The lowest energy models were examined by eye to ensure that the model fitted into the density, the protomer was placed into the context of the whole structure and the Rosetta Relax protocol was run on the full complex.

Rosetta enumerative sampling (RosettaES) was used to build in the IGL loops and NT loops de novo for each protomer[79]. The ClpA residues 612–628 were deleted from each protomer and RosettaES was run to rebuild the loops with a beam width of 32. The resulting model with rebuilt IGL loops was added into the full model and the Rosetta Relax protocol was run. Residues 16–32 from ClpP were deleted from each protomer and the same RosettaES parameters were used to build in the NT loops, followed by the Rosetta Relax protocol.

Reporting Summary. Further information on research design is available in the Nature Research Reporting Summary linked to this article.

Data availability

ClpAP cryo-EM maps and atomic coordinates have been deposited in the EMDB and PDB with accession codes EMD-21519 and PDB 6W1Z for ClpAP^{Eng1}; EMD-21520 and PDB 6W20 for ClpAP^{Dis}; EMD-21521 and PDB 6W21 for ClpAP^{Eng2}; EMD-21522 and PDB 6W22 for ClpAP^{Eng1} focus; EMD-21523 and PDB 6W23 for ClpAP^{Dis} focus; EMD-21524 and PDB 6W24 for ClpAP^{Eng2} focus; EMD-20851 and PDB 6UQO for ATPγS-ClpAP^{Eng}; and EMD-20845 and PDB 6UQE for ATPγS-ClpAP^{Dis}. Uncropped images for Extended Data Fig. 1a,c are provided as Source Data online.

References

67. Veronese, P. K., Stafford, R. P. & Lucius, A. L. The *Escherichia coli* ClpA molecular chaperone self-assembles into tetramers. *Biochemistry* **48**, 9221–9233 (2009).
68. Zheng, S. et al. MotionCor2: anisotropic correction of beam-induced motion for improved cryo-electron microscopy. *Nat. Methods* **14**, 331–332 (2017).
69. Punjani, A., Rubinstein, J. L., Fleet, D. J. & Brubaker, M. A. cryoSPARC: algorithms for rapid unsupervised cryo-EM structure determination. *Nat. Methods* **14**, 290–296 (2017).
70. Waterhouse, A. et al. SWISS-MODEL: homology modelling of protein structures and complexes. *Nucleic Acids Res.* **46**, W296–W303 (2018).
71. Pettersen, E. F. et al. UCSF Chimera–a visualization system for exploratory research and analysis. *J. Comput. Chem.* **25**, 1605–1612 (2004).
72. Afonine, P. V. et al. Real-space refinement in PHENIX for cryo-EM and crystallography. *Acta Crystallogr. D Struct. Biol.* **74**, 531–544 (2018).
73. Emsley, P., Lohkamp, B., Scott, W. G. & Cowtan, K. Features and development of Coot. *Acta Crystallogr. D Biol. Crystallogr.* **66**, 486–501 (2010).
74. Moriarty, N. W., Grosse-Kunstleve, R. W. & Adams, P. D. electronic Ligand Builder and Optimization Workbench (eLBOW): a tool for ligand coordinate and restraint generation. *Acta Crystallogr. D Biol. Crystallogr.* **65**, 1074–1080 (2009).
75. DiMaio, F. et al. Atomic-accuracy models from 4.5-Å cryo-electron microscopy data with density-guided iterative local refinement. *Nat. Methods* **12**, 361–365 (2015).
76. Song, Y. et al. High-resolution comparative modeling with RosettaCM. *Structure* **21**, 1735–1742 (2013).
77. Xia, D., Esser, L., Singh, S. K., Guo, F. & Maurizi, M. R. Crystallographic investigation of peptide binding sites in the N-domain of the ClpA chaperone. *J. Struct. Biol.* **146**, 166–179 (2004).
78. Zimmermann, L. et al. A completely reimplemented MPI bioinformatics toolkit with a new HHpred server at its core. *J. Mol. Biol.* **430**, 2237–2243 (2018).
79. Frenz, B., Walls, A. C., Egelman, E. H., Veesler, D. & DiMaio, F. RosettaES: a sampling strategy enabling automated interpretation of difficult cryo-EM maps. *Nat. Methods* **14**, 797–800 (2017).

Acknowledgements

We thank K. Mack, Z. March, R. Cupo, T. Pospiech and J. Braxton for feedback on the manuscript. We thank the UCSF BACEM Facility for assistance with data collection.

This work was supported by an Alzheimer's Association Research Fellowship (to J.B.L.), a GAANN fellowship (to A.N.R.), NSF grant no. MCB-1412624 (to A.L.L.) and NIH grant nos. R01GM099836 (to J.S.) and R01GM110001 (to D.R.S.).

Author contributions

K.E.L. and A.N.R. carried out all experiments, refinement and modeling procedures for structure determination; developed figures; and wrote and edited the manuscript. E.T. operated the Krios microscope and helped with data collection. J.B.L. performed biochemical substrate-binding experiments. N.W.S. expressed and purified protein components. A.C.T. performed degradation assays. A.L.L. and J.S. wrote and edited the manuscript. D.R.S. designed and supervised the project and wrote and edited the manuscript.

Competing interests

The authors declare no competing interests.

Additional information

Extended data is available for this paper at https://doi.org/10.1038/s41594-020-0409-5.

Supplementary information is available for this paper at https://doi.org/10.1038/s41594-020-0409-5.

Correspondence and requests for materials should be addressed to D.R.S.

Peer review information Inês Chen was the primary editor on this article and managed its editorial process and peer review in collaboration with the rest of the editorial team.

Reprints and permissions information is available at www.nature.com/reprints.

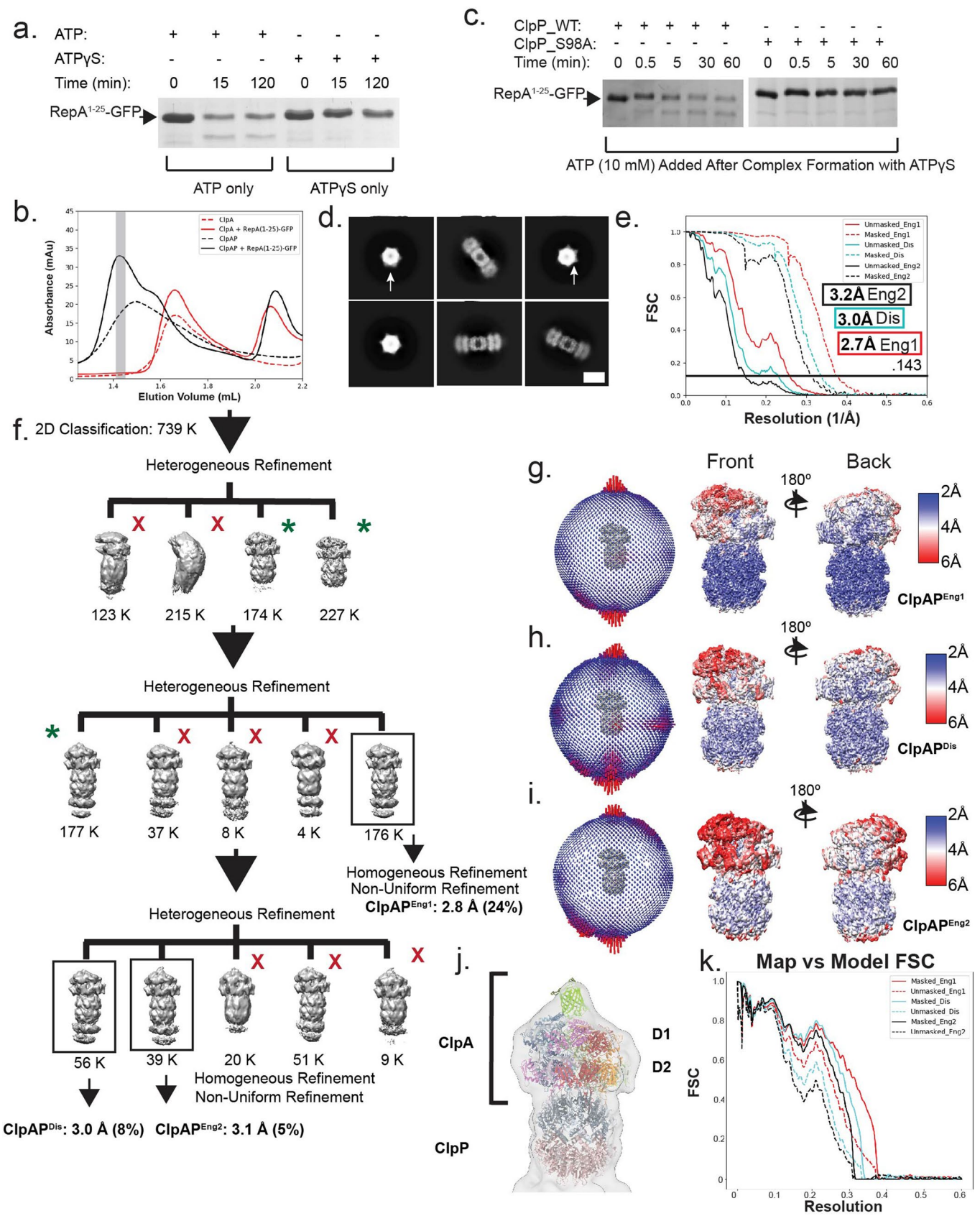

Extended Data Fig. 1 | See next page for caption.

Extended Data Fig. 1 | ClpAP complex formation with RepA(1-25)-GFP and cryoEM data analysis. a $RepA^{1-25}$-GFP degradation assay in the presence of either ATPγS or ATP along with ClpA and ClpP. The assay was performed at 20°. Arrow represents RepA degradation product. **b** Size exclusion chromatography (SEC) trace of the components and formed ClpAP complex following incubation with $RepA^{1-25}$-GFP and ATPγS. The 280 absorbance traces are shown for ClpA alone (red, dashed), ClpA with $RepA^{1-25}$-GFP (red, solid), ClpAP alone (black, dashed) and ClpAP with $RepA^{1-25}$-GFP (black, solid). **c** $RepA^{1-25}$-GFP degradation assay in the presence of ATPγS with both ClpP WT and ClpP_S98A. ATP was spiked into the reaction at 10 mM after the initial complex formation for 15 min was completed with ATPγS. The zero-time point is before spiking ATP into the reaction. The assay was performed at 20°. **d** Reference-free 2D class averages of ClpAP bound to $RepA^{1-25}$-GFP. The scale bar equals 125 Å. **e** Gold standard FSC-curves for the final refinement of $ClpAP^{Eng1}$(red), $ClpAP^{Dis}$(cyan), $ClpAP^{Eng2}$(black) of the ClpAP-RepA(1-25)-GFP complex. **f** 3D classification scheme used to identify the two different states in the ClpAP-$RepA^{1-25}$-GFP dataset. Green asterisk represents the classes in which the particles were pooled together for further classification and refinement. The local resolution map of $ClpAP^{Eng-1}$ (**g**), $ClpAP^{Dis}$ (**h**) and $ClpAP^{Eng-2}$ (**i**). **j** Low-pass filtered map showing globular density docked with GFP (PDB 1GFL) and additional N-terminal ClpA density (NTD). **k** Map vs. Model FSC of $ClpAP^{Eng1}$(red), $ClpAP^{Dis}$(cyan), $ClpAP^{Eng2}$ (black) of the ClpAP-RepA(1-25)-GFP complex following atomic modeling in Rosetta. Uncropped gel images are available as source data online.

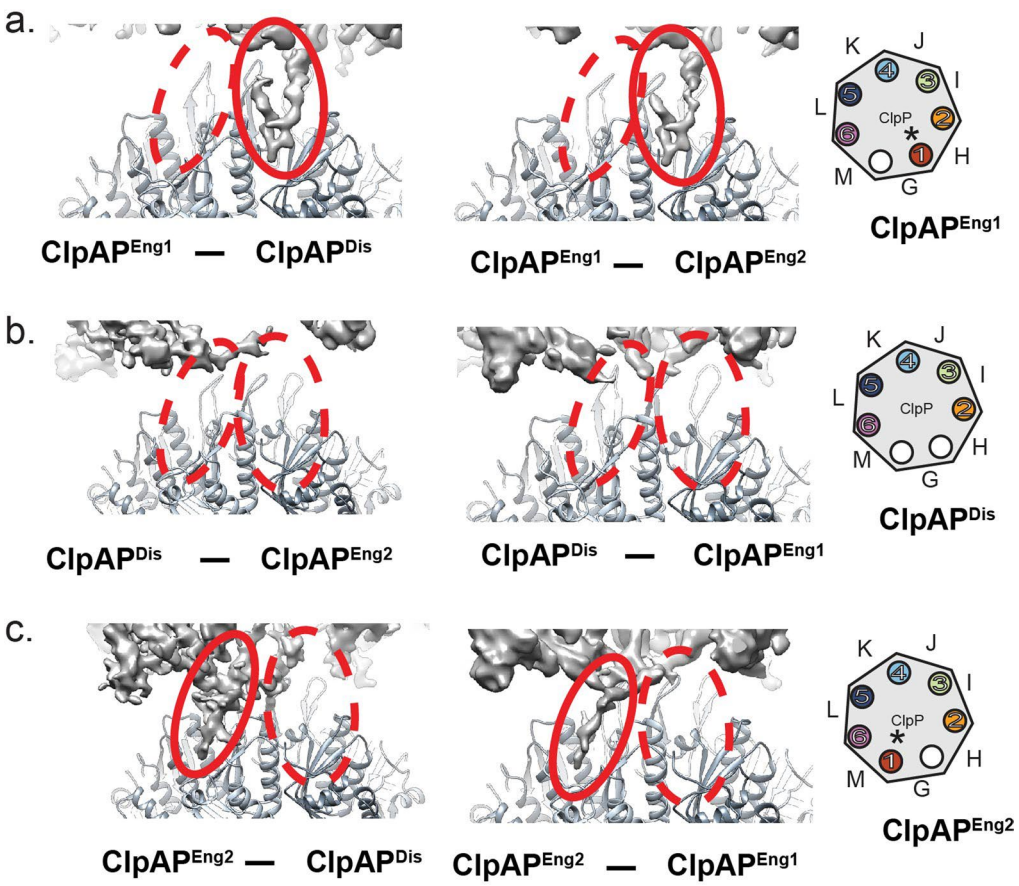

Extended Data Fig. 2 | Difference maps of the ClpAP interface. Difference maps of the cryo-EM maps of **a** $ClpAP^{Eng1}$ vs. $ClpAP^{Dis}$ and $ClpAP^{Eng-2}$, **b** $ClpAP^{Dis}$ vs. $ClpAP^{Eng-1}$ and $ClpAP^{Eng-2}$, **c** $ClpAP^{Eng-2}$ vs. $ClpAP^{Dis}$ and $ClpAP^{Eng-1}$. The IGL pockets are encompassed by red circle, open pocket (dashed) and occupied pocket (solid). Schematic (right) shows occupancy of the ClpA IGL-loops (circles, colored and numbered by protomer) around the ClpA hexamer, with the empty IGL pockets (white circles) and ClpA protomers indicated (letters) for the different states. Asterisk represents the IGL-loop that is engaging in that state.

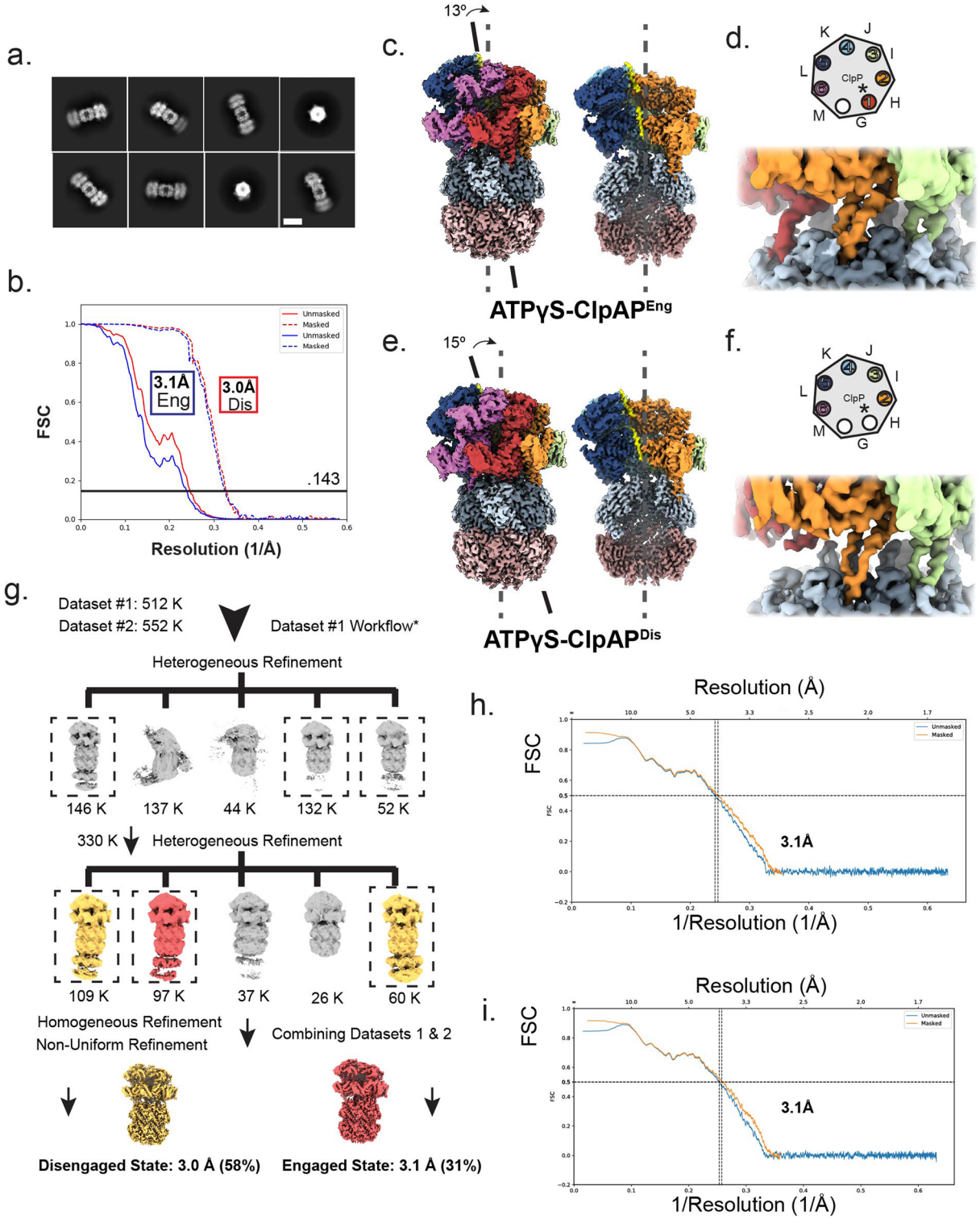

Extended Data Fig. 3 | ATPγS-ClpAP cryoEM data analysis. a Reference-free 2D class averages of ClpAP-γS bound to RepA$^{1-25}$-GFP. The scale bar equals 125 Å. **b** Gold standard FSC-curves for the final refinement of ATPγS-ClpAP^{Eng} (blue) and ATPγS-ClpAP^{Dis} (red) of the ClpAP-RepA(1-25)-GFP complex. ATPγS-ClpAP^{Eng1} (**c**) and ATPγS-ClpAP^{Dis} (**d**) cryo-EM maps showing degree offset (arrow) of the ClpA channel axis (solid line) and substrate position (yellow density) compared to the ClpP pore and proteolytic chamber (dashed line). Schematic (below,left) shows occupancy of the ClpA IGL-loops (circles, colored and numbered by protomer) around the ClpA hexamer, with the empty IGL pockets (white circles) and ClpA protomers indicated (letters) for the different states. **e** 3D classification scheme used to identify the two different states in the ATPγS-ClpAP-RepA$^{1-25}$-GFP dataset. Dotted boxes represent the classes in which the particles were pooled together for further classification and refinement. The maps for ClpAP^{Eng} (red) and ClpAP^{Dis} (yellow) are colored accordingly. Map vs. Model FSC of ATPγS-ClpAP^{Eng}(**f**) and ATPγS-ClpAP^{Dis}(**g**) following atomic modeling in Rosetta.

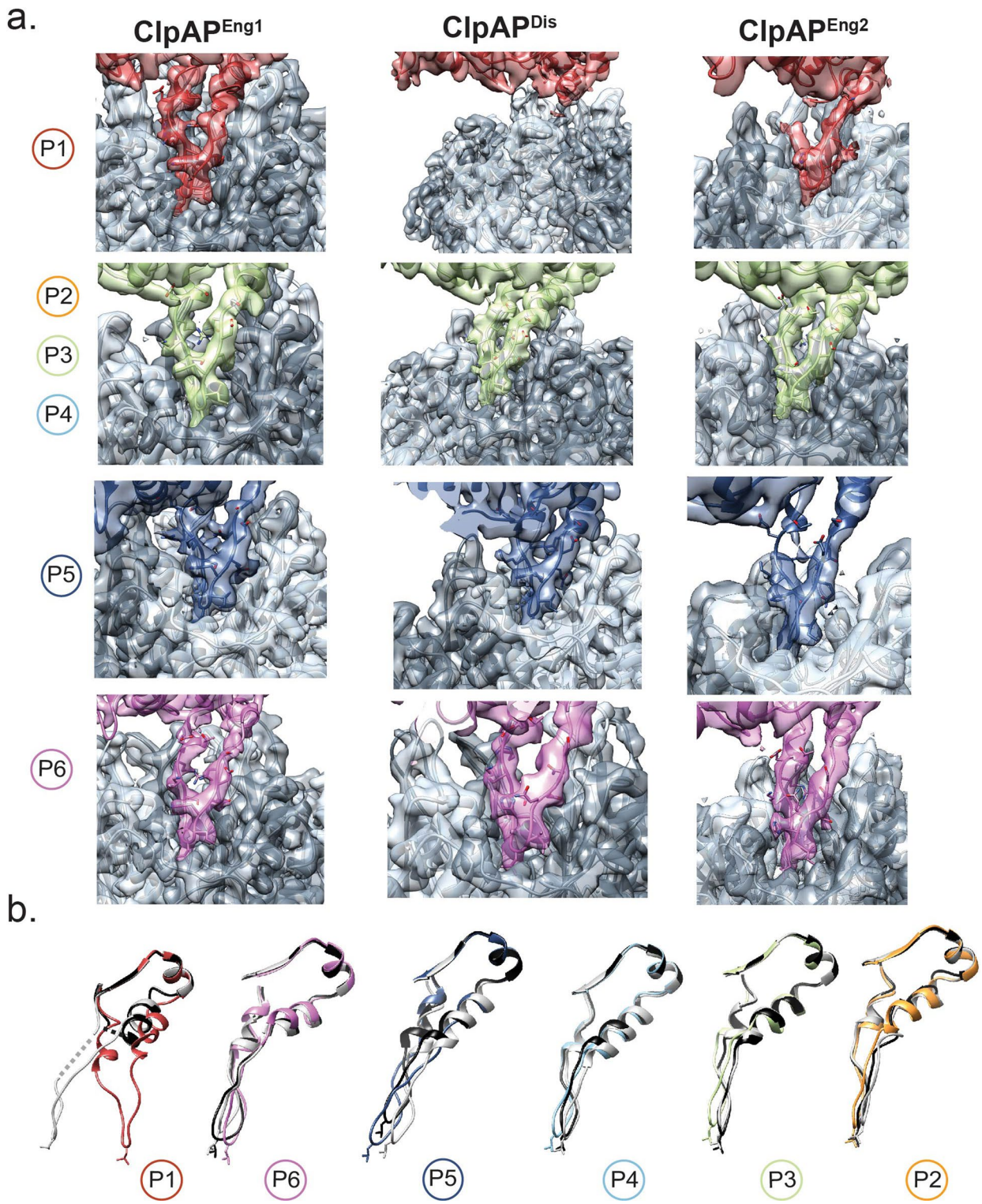

Extended Data Fig. 4 | Comparison of IGL loops between the different states. a EM map and model of the IGL-loop in the hydrophobic pocket of P1 (top), P2-P4 (middle, top), P5 (middle, bottom) and P6 (bottom) for ClpAP^{Eng1}(left), ClpAP^{Dis} (middle) and ClpAP^{Eng2} (right). **b** Overlay of IGL-loops of ClpAP^{Eng1} (colored by protomer) vs. ClpAP^{Dis} (black) vs. ClpAP^{Eng2} (grey) laid out after alignment to the residues (638-649) above the IGL-loop. The dotted loop in P1 represents the missing loop in ClpAP^{Dis} and ClpAP^{Eng-2}.

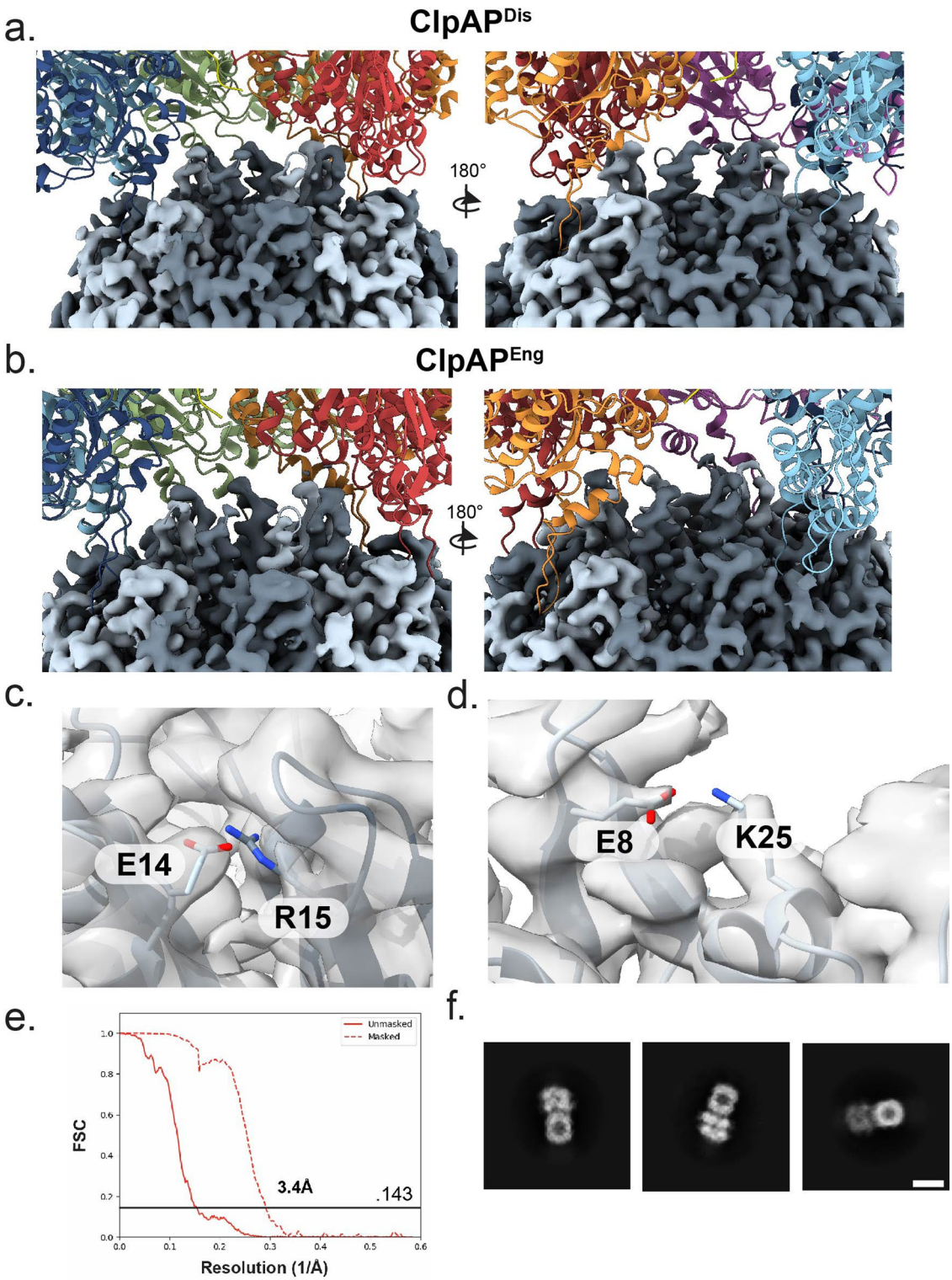

Extended Data Fig. 5 | Single capped ClpAP structure and ClpP N-terminal loop interactions. a Map of the ClpP N-terminal gating loops and the model for ClpA with substrate for ClpAP^{Dis} (**b**) ClpAP^{Eng}. Map and model view of ClpP residues E14 and R15 (**c**) and E8 and K25 (**d**). **e** Gold standard FSC curve and (**f**) 2D reference-free class averages of the single capped ClpAP structure.

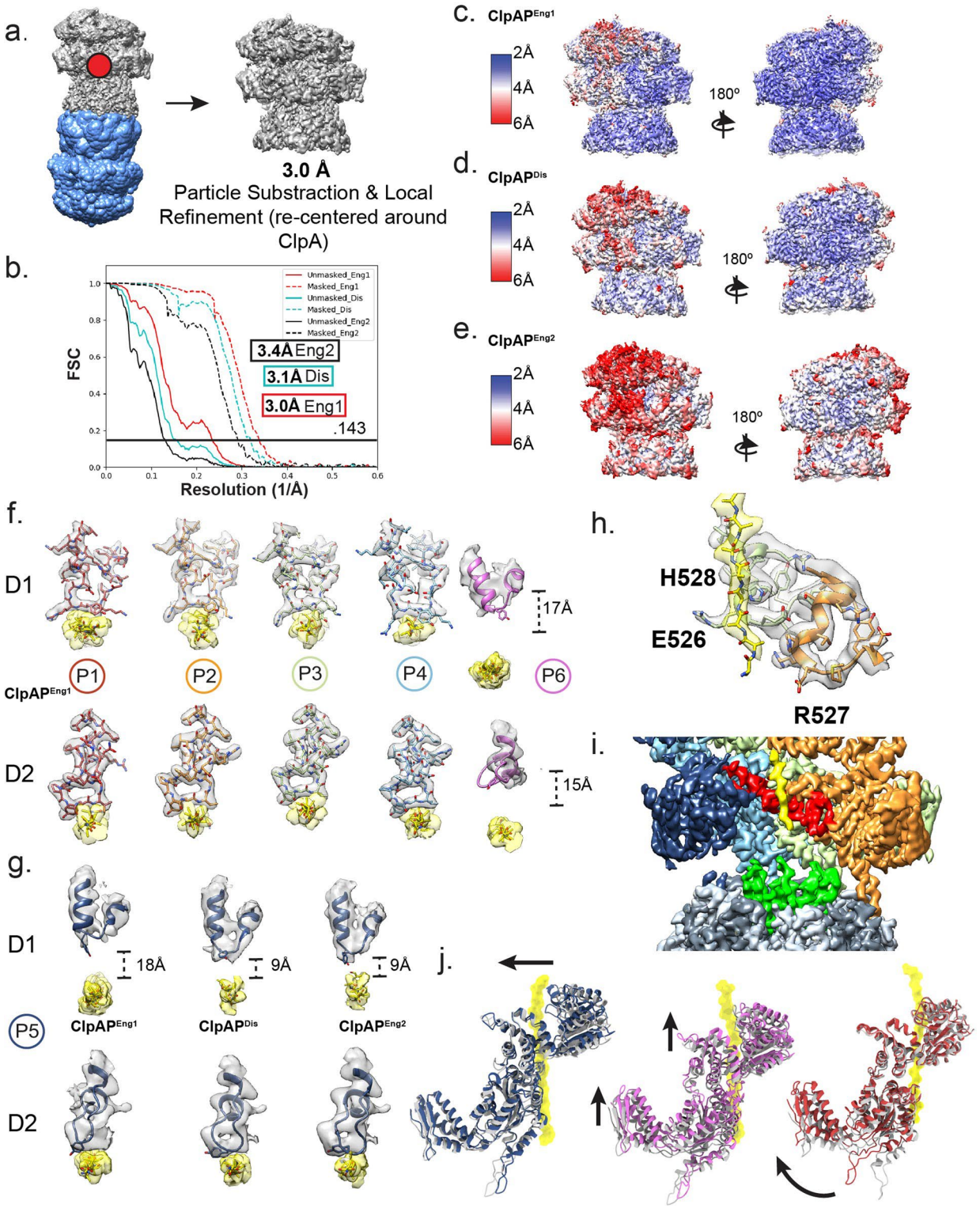

Extended Data Fig. 6 | Particle Subtraction and Focus Refinement of ClpAP^{Eng1}, ClpAP^{Eng2} and ClpAP^{Dis}. **a** EM map with mask (grey) used for particle subtraction of ClpA. Red dot represents the point in which particles were shifted to. **b** Gold standard FSC curve of both focus maps for ClpAP^{Eng1} (red), ClpAP^{Dis} (cyan), and ClpAP^{Eng2} (black). The local resolution map of ClpAP^{Eng1} (**c**), ClpAP^{Dis} (**d**) and ClpAP^{Eng2} (**e**). **f** EM map and model of each Tyr-containing pore loop in ClpAP^{Eng1} for both D1 (top) and D2 (bottom), the substrate channel density is colored yellow. **g** EM map and model of each Tyr-containing pore loop in P5 for ClpAP^{Eng1} (left), ClpAP^{Dis} (middle), and ClpAP^{Eng2} (right) for both D1 (top) and D2 (bottom), the substrate channel density is colored yellow. The distance between the Tyr and the substrate is represented by dotted line. **h** EM map and model of ClpAP^{Eng1} (colored by protomer) with the D2 secondary pore loops residues interacting with substrate. **i** ClpAP^{Eng1} EM map colored by protomer with D2 secondary pore loops (red) and ClpP NTD-loops (green). **j** Overlay of the seam protomers P5 (left), P1 (middle), and P6 (right) for ClpAP^{Eng1} (grey) and ClpAP^{Eng2} (colored) showing conformational shifts (arrows) supporting translocation step.

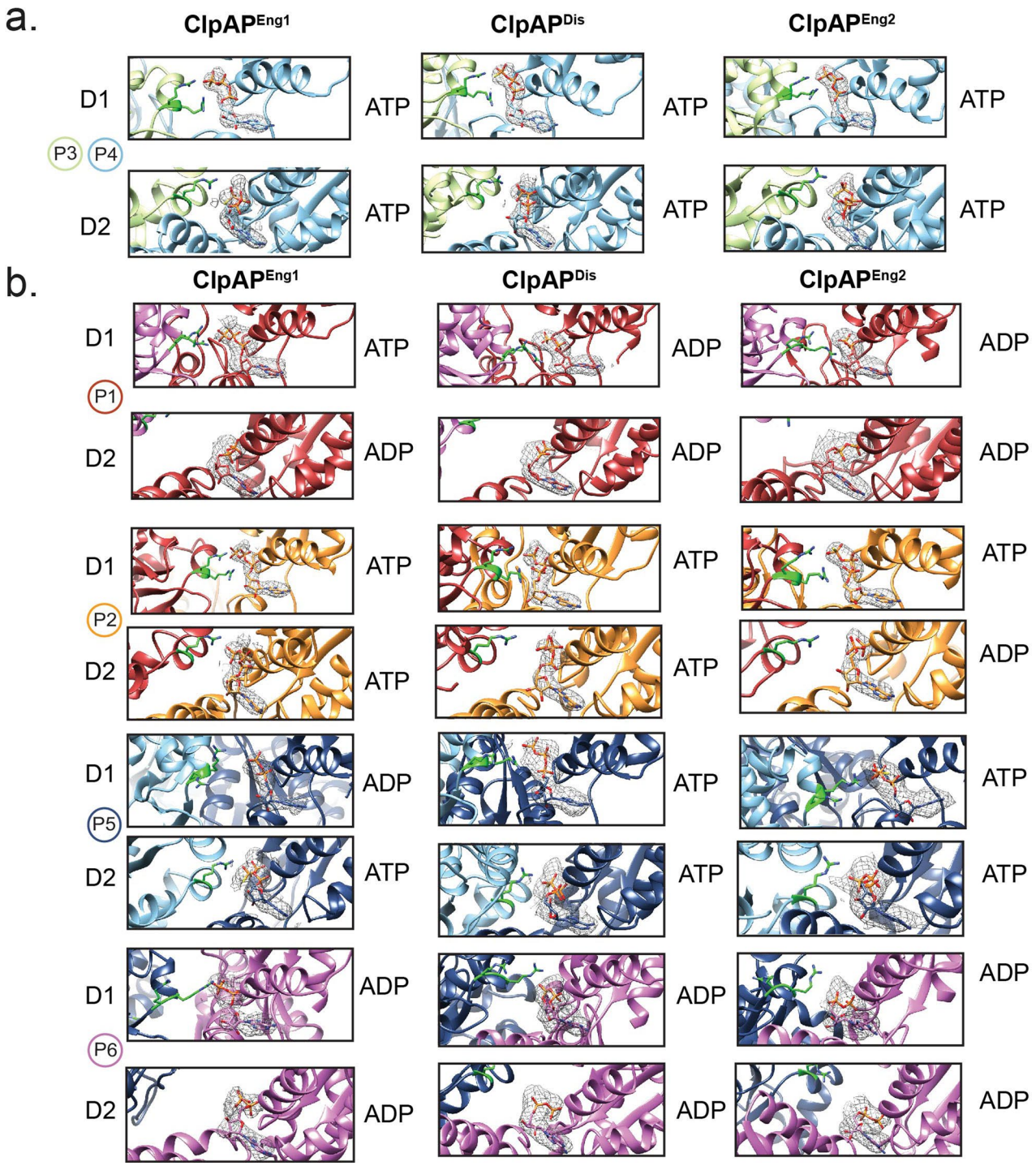

Extended Data Fig. 7 | Nucleotide States of ClpAP^{Eng1}, ClpAP^{Eng2} and ClpAP^{Dis}. a Difference map density for P4 D1 and D2 ATP with Arg finger residues displayed in green. There are no differences between P3 and P4, therefore P3 ATP density is not shown. **b** Difference map density for P1, P2, P5 and P6 for both D1 and D2 and Arg finger residues colored green.

nature research

Corresponding author(s): Southworth, Daniel R.

Last updated by author(s): Oct 23, 2019

Reporting Summary

Nature Research wishes to improve the reproducibility of the work that we publish. This form provides structure for consistency and transparency in reporting. For further information on Nature Research policies, see Authors & Referees and the Editorial Policy Checklist.

Statistics

For all statistical analyses, confirm that the following items are present in the figure legend, table legend, main text, or Methods section.

n/a	Confirmed
☐	☒ The exact sample size (*n*) for each experimental group/condition, given as a discrete number and unit of measurement
☐	☒ A statement on whether measurements were taken from distinct samples or whether the same sample was measured repeatedly
☒	☐ The statistical test(s) used AND whether they are one- or two-sided *Only common tests should be described solely by name; describe more complex techniques in the Methods section.*
☒	☐ A description of all covariates tested
☒	☐ A description of any assumptions or corrections, such as tests of normality and adjustment for multiple comparisons
☒	☐ A full description of the statistical parameters including central tendency (e.g. means) or other basic estimates (e.g. regression coefficient) AND variation (e.g. standard deviation) or associated estimates of uncertainty (e.g. confidence intervals)
☒	☐ For null hypothesis testing, the test statistic (e.g. *F*, *t*, *r*) with confidence intervals, effect sizes, degrees of freedom and *P* value noted *Give P values as exact values whenever suitable.*
☒	☐ For Bayesian analysis, information on the choice of priors and Markov chain Monte Carlo settings
☒	☐ For hierarchical and complex designs, identification of the appropriate level for tests and full reporting of outcomes
☒	☐ Estimates of effect sizes (e.g. Cohen's *d*, Pearson's *r*), indicating how they were calculated

Our web collection on statistics for biologists contains articles on many of the points above.

Software and code

Policy information about availability of computer code

Data collection	N/A
Data analysis	NA

For manuscripts utilizing custom algorithms or software that are central to the research but not yet described in published literature, software must be made available to editors/reviewers. We strongly encourage code deposition in a community repository (e.g. GitHub). See the Nature Research guidelines for submitting code & software for further information.

Data

Policy information about availability of data

All manuscripts must include a data availability statement. This statement should provide the following information, where applicable:

- Accession codes, unique identifiers, or web links for publicly available datasets
- A list of figures that have associated raw data
- A description of any restrictions on data availability

Final sharpened cryo-EM density maps and corresponding atomic models are deposited in the Electron Microscopy Data Bank and the Protein Data Bank with the following accession codes: EMD-20845 and PDB 6UQE for ClpAP-Disengaged, EMD-20852 and PDB 6UQP for ClpA-Disengaged Focus, EMD-20185 and PDB 6UQO for ClpAP-Engaged, and EMD-20848 and PDB 6UQH for ClpA-Engaged focus.

Field-specific reporting

Please select the one below that is the best fit for your research. If you are not sure, read the appropriate sections before making your selection.

☒ Life sciences ☐ Behavioural & social sciences ☐ Ecological, evolutionary & environmental sciences

For a reference copy of the document with all sections, see nature.com/documents/nr-reporting-summary-flat.pdf

Life sciences study design

All studies must disclose on these points even when the disclosure is negative.

Sample size	Sample size determined by particle number and listed in Supplementary Table 1
Data exclusions	Particles were excluded during classification and refinement process based on 2D and 3D analysis. Initial and final particle numbers are included in Supplementary Table 1
Replication	Cryo-EM sample preparation and data collection was performed in duplicate
Randomization	N/A
Blinding	N/A

Reporting for specific materials, systems and methods

We require information from authors about some types of materials, experimental systems and methods used in many studies. Here, indicate whether each material, system or method listed is relevant to your study. If you are not sure if a list item applies to your research, read the appropriate section before selecting a response.

Materials & experimental systems

n/a	Involved in the study
☒	☐ Antibodies
☒	☐ Eukaryotic cell lines
☒	☐ Palaeontology
☒	☐ Animals and other organisms
☒	☐ Human research participants
☒	☐ Clinical data

Methods

n/a	Involved in the study
☒	☐ ChIP-seq
☒	☐ Flow cytometry
☒	☐ MRI-based neuroimaging